






On Identifying and Mitigating Bias in Inferred Measurements for Solar Vector Magnetic Field Data.

K.D. Leka^{1,2}  · Eric L. Wagner¹  · Ana Belén Griñón-Marín^{3,4,5}  · Véronique Bommier⁶  · Richard Higgins⁷ 

© Springer

Abstract The problem of bias, meaning over- or underestimation, of the component perpendicular to the line-of-sight (B_{\perp}) in vector magnetic field maps is discussed. Previous works on this topic have illustrated that the problem exists; here we perform novel investigations to quantify the bias, fully understand its source(s), and provide mitigation strategies. First, we develop quantitative metrics to measure the B_{\perp} bias and quantify the effect in both local (physical) and native image-plane components. Second we test and evaluate different in-

✉ K.D. Leka
leka@nwra.com
E.L. Wagner
wagneric@nwra.com
A. B. Griñón-Marín
a.b.g.marin@astro.uio.no
V. Bommier
v.bommier@obspm.fr
R. Higgins
relh@umich.edu

- ¹ NorthWest Research Associates, Boulder, Colorado, USA
- ² Institute for Space-Earth Environmental Research, Nagoya University, Nagoya, Aichi, Japan
- ³ W. W. Hansen Experimental Physics Laboratory, Stanford University, Stanford, California, USA
- ⁴ Institute of Theoretical Astrophysics, University of Oslo, Blindern, Oslo, Norway
- ⁵ Rosseland Centre for Solar Physics, University of Oslo, Blindern, Oslo, Norway
- ⁶ LESIA, Observatoire de Paris, Université PSL, Sorbonne Université, Université Paris Cité, CNRS, Meudon, France
- ⁷ University of Michigan, Ann Arbor, Michigan, USA

version options and data sources, to systematically characterize the impacts of choices, including explicitly accounting for the magnetic fill fraction ff . Third we deploy a simple model to test how noise and different models of the bias may manifest. From these three investigations we find that while the bias is dominantly present in under-resolved structures, it is also present in strong-field pixel-filling structures. Noise in the magnetograms can exacerbate the problem, but it is not the primary cause. We show that fitting ff explicitly provides significant mitigation, but that other considerations such as choice of χ^2 weights and optimization algorithms can impact the results as well. Finally, we demonstrate a straightforward “quick fix” that can be applied *post-facto* but prior to solving the 180° ambiguity in B_\perp , and which may be useful when global-scale structures are, *e.g.*, used for model boundary input. The conclusions of this work support the deployment of inversion codes that explicitly fit ff or, as with the new **SynthIA** neural-net, that are trained on data that did so.

Keywords: Instrumental Effects; Magnetic fields, Photosphere; Polarization, Optical

1. Introduction

It is a challenging problem to infer the magnetic field strength and direction in the solar photosphere as it threads a dynamic plasma (see del Toro Iniesta and Ruiz Cobo, 2016, and references therein). The assumptions of a Milne-Eddington (ME) atmosphere provide a good estimate of the average strength and direction across the layers where magnetically-sensitive photospheric spectral lines are formed (Westendorp Plaza et al., 1998), especially in structures where a single pixel-filling magnetic component is present or at least dominates. Under-resolved multiple atmospheres (whether all magnetized or not) contributing light to the resolution element result in polarimetric signals that are intensity-weighted averages of the contributing atmospheres (Sanchez Almeida, 1997; Leka and Barnes, 2012) which rarely resemble expected ME Stokes spectra (even without complications from unresolved velocity components or gradients within the line-forming region).

The treatment of instrumental scattered light, and the approach used to estimate relative contributions of magnetized *vs.* unmagnetized incoming light (the magnetic “fill fraction”, ff , or percentage of a pixel filled by magnetic field) will influence the inferred nature of magnetic structures, especially (but not solely) unresolved structures (Lites et al., 1996; Socas Navarro, 2004; LaBonte, 2004; Orozco Suárez and Katsukawa, 2012; del Toro Iniesta, Orozco Suárez, and Bellot Rubio, 2010; Leka and Barnes, 2012; Bommier, 2016; Sainz Dalda, 2017). The particulars of how inversion techniques are invoked by which to infer the magnetic field from the spectropolarimetric data, even “standard” Milne-Eddington inversions, will influence the results. The “particulars” can include the number and which spectral lines are used, plus mundane-seeming choices of optimization algorithms, stopping conditions, and any optimization weighting applied to χ^2 calculation (see, *e.g.* Centeno et al., 2014; Sainz Dalda, 2017, for discussion).

As has been introduced at length in Pevtsov et al. (2021); Liu et al. (2022), with vector polarimetry and inversions covering the full visible solar disk from, *e.g.*, the Vector SpectroMagnetograph (VSM Keller and The SOLIS Team, 2001; Henney, Keller, and Harvey, 2006) of the Synoptic Optical Long-term Investigations of the Sun facility (<https://nso.edu/telescopes/nisp/solis/>) and now the Helioseismic and Magnetic Imager (HMI Scherrer et al., 2012; Schou et al., 2012; Centeno et al., 2014; Hoeksema et al., 2014) on the Solar Dynamics Observatory (*SDO*; Pesnell, Thompson, and Chamberlin, 2012), there is the capability of estimating the vector-components of the photospheric magnetic field over large areas of the Sun. Unfortunately, as demonstrated recently (Rudenko and Dmitrienko, 2018; Pevtsov et al., 2021; Sun et al., 2021; Liu et al., 2022), large-scale magnetic structures can present behavior that is physically unexpected. Specifically, a preferred direction in polar fields or a “flip” in the direction of the zonal-directed (East/West) horizontal component of magnetic structures upon crossing the central meridian. Given that the opposite signs of this bias are present in data from different facilities (Pevtsov et al., 2021; Sun et al., 2021), the problem is solidified as originating from instrumentation, data preparation, and/or inversion, rather than being solar in origin. We explore these options further, below.

What has not been emphasized yet is the impact on physical interpretation. The over-estimation of the transverse component B_{\perp} contributes to the inferred physical components $[B_x^h, B_y^h, B_z^h]$, or heliographic / local components of the field vector, in a non-linear way according to the inherent underlying structure as well the viewing angle θ (*i.e.* the structure’s location on the solar disk).

It has been proposed that the most susceptible features are those which are unresolved. As hypothesized in Pevtsov et al. (2021) and demonstrated in Liu et al. (2022), including the magnetic fill fraction ff explicitly as part of a Milne-Eddington solution changes the inferred field vector, such that the bias may be mitigated substantially. This is not a new point (Ronan, Mickey, and Orrall, 1987; Lites and Skumanich, 1990; LaBonte, 2004; Bommier et al., 2007; del Toro Iniesta, Orozco Suárez, and Bellot Rubio, 2010; Sainz Dalda, 2017). Forcing the magnetic fill fraction $ff = 1.0$ for unresolved structures is likely the dominant source of this bias; as shown in Liu et al. (2022), correcting this assumption by invoking a new version of the Very Fast Inversion of Stokes Vector Milne-Eddington approach (Borrero et al., 2010; Centeno et al., 2014; Griñón-Marín et al., 2021) can mitigate the magnitude of the bias. However, as also shown in (Pevtsov et al., 2021), the magnitude of the photon noise can contribute. Spatial integrity, field of view, and cadence are all drivers of instrument design, the outcomes of which are as different as the questions they are optimized to answer *c.f.* the *SDO*/HMI *vs.* the *Hinode* SpectroPolarimeter (Lites et al., 2013), and we use both *SDO*/HMI and *Hinode*/SP to investigate not just fill-fraction fitting, but noise, instrument, data specifics, and inversion implementation.

Most importantly we present quantitative metrics by which to evaluate the extent and direction of the bias¹ and the contributing factors, and finally demon-

¹The authors became aware of Rudenko and Dmitrienko (2018) effectively after this paper was accepted. We want to acknowledge some similarities of our approach to theirs, state that

strate one “quick and dirty” correction which is shown to mitigate (although not necessarily completely correct) the bias in any data for which certain structures are observed and good coverage in observing angle is available.

We begin the methodology section (§ 2) with a description of the data, target acquisition, and analysis methods and evaluation metrics, plus a description of a simple model used in the investigation. This is followed by a summary of results (§ 3) and finally a demonstration of a rudimentary correction approach (§ 4) for when the option of re-inverting the data is not available.

2. Methodology

In this section we present the algorithms for selecting features, the observational targets and analysis methodology.

The overall issue for *SDO*/HMI pipeline output is that the inferred component in plane-of-sky is stronger than it “should be” compared to the line-of-sight component, most apparently those with unresolved magnetic structure, *i.e.* $ff < 1.0$. For data from the Synoptic Optical Long-Term Investigations of the Sun (SO-LIS) Vector-SpectroMagnetograph (VSM; Keller and The SOLIS Team, 2001), according to Pevtsov et al. (2021), it is weaker than it “should be”. We refer to this as the bias in B_{\perp} but also refer to the image-plane (as returned from the inversion) inclination $\gamma^i \in [0^\circ, 180^\circ]$ where $[90^\circ]$ is in the plane-of-the-sky. In some cases, the “polarity” of $B_{\parallel} = B_{\text{los}}$ is inconsequential or adds confusion, in which case we limit the inclination, referred to as $|\gamma^i| \in [0^\circ, 90^\circ]$. Throughout, while we may discuss ff as distinct from the field magnitude B , it is their product that is evaluated.

2.1. Target Features

Solar plage is generally agreed to be comprised of kilo-Gauss concentrations of predominantly radially-directed field; generally not strong enough to form a continuum depression (but magnetic and thermal impacts are sufficient to produce continuum-intensity enhancements when viewed at an angle), the small size of these concentrations means they are rarely resolved with today’s instruments. Plage areas are not inherently “weak field” (*c.f.* the “magnetic knots” in Rudenko and Dmitrienko (2018)). The inability to resolve the structures leads to a canonical area-averaged (pixel-averaged) flux density estimate for plage of $1\text{--}few \times 100 \text{ Mx cm}^{-2}$, depending on instrument specifics. Plage is a wide-spread source for “global-scale” solar magnetic field structure, and contributes strongly to synoptic (or synodic) full-sun magnetic maps.

The overall approach we take relies on the analysis of structures on the sun where the magnetic inclination is known, at least on a statistical basis: plage regions, and the darkest umbrae of very stable sunspots. These two targets, when carefully selected, should be dominated by radially-directed field (for *SDO*/HMI

the approaches were developed independently, and direct interested readers to that paper for salient points.

spatial resolution and spectral sampling and sensitivity). It is not required that the inclination be *only* radial, just that it be *dominated* by radially-directed field.

In cases where full-disk data are not available, there is an additional assumption invoked, that these structures would display minimal large-scale variation over the course of days, again on a statistical basis (for appropriately stable sunspots).

Different between these two structures are the magnetic fill fraction, with the darkest umbrae of sunspots presenting field-filled pixels ($ff = 1.0$), whereas plage should present un-resolved bundles of field within field-free (or field-less) plasma ($ff < 1.0$). Both plage and sunspots generally present polarization signals well above the noise. The two types of features appropriate for this analysis are selected thus:

i: The very central darkest portions of sunspot umbrae in spots that are large and not evolving noticeably. To select these areas,

i. 1) Determine that the size, complexity, morphology and evolution of the target sunspot is large, nonexistent, round and steady, respectively.

i. 2) Create four masks:

- o Mask 1, Continuum intensity: select the darkest points within sunspot umbrae. Specifically, for *Hinode*/SP data: an $I_c/\text{median}(I_c)$ limited-FOV image is smoothed with a 4-pixel boxcar, and those pixels < 0.4 are selected; for *SDO*/HMI: using I^* normalized continuum intensity from the `hmi.Ic_nolimbdark_720s` data series (see Hoeksema et al., 2014, for a description of the different data series available from the *SDO*/HMI pipeline products), choose pixels with $I^* < 0.2$. The resulting mask is then “dilated” by a 2×2 box.
- o Mask 2, Field Strength: $ffBB > 200$; tests showed that this level consistently retains plage areas but does not include noise across orbital variations in *SDO*/HMI data. This mask is then “eroded” by a 2×2 box to remove single-pixel detections.
- o Mask 3, Inclination: An image of the “local” or heliographic (or “physical”) $|\gamma^h|$ is created, smoothed using a 4-pixel boxcar, and pixels $< 30^\circ$ are identified; this mask is then subjected to first being eroded and then grown both using a 2×2 box.
- o Mask 4, Data Quality: for *SDO*/HMI, mask to include only those pixels with `conf = 0.0` from the `confid_map.fits` segment of `hmi.ME_720s_fd10` series, indicating no failures in data quality or inversion (convergence, etc.). For *Hinode*/SP: only those pixels with total polarization $P > 0.4\%$; those below are used for computing the non-magnetic spectral profiles. For all: within $\mu = \cos(\theta) > 0.35$ (within $\approx 70^\circ$ from disk center).

i. 3) The four masks are added together and only pixels where all conditions are satisfied are selected.

ii: Plage areas are found either in the vicinity of a sunspot, or as active-region remnants that can cover many degrees of the disk. Arguably, any individual

plage element evolves, but statistically speaking their distribution is not expected to differ due the hemisphere in which they are located. To select these areas,

- ii. 1: Again, construct a series of independent masks:
 - Mask 1, Continuum Intensity: where $I_c/\text{median}(I_c) > 0.9$ (*Hinode*/SP) or $I^* > 0.9$ (*SDO*/HMI).
 - Mask 2, Field Strength: as per Mask 2 above, but additionally grown with a 2×2 box to ensure coverage of plage concentrations.
 - Mask 3, Inclination: same ask Mask 3, above.
 - Mask 4, Data Quality: same as Mask 4, above.
 - Mask 5, extended sunspot / super-penumbral exclusion: using continuum intensity, select all sunspot points by $I_c/\text{median}(I_c) < 0.9$ (*Hinode*/SP) or $I^* < 0.9$ (*SDO*/HMI). Erode the result using a 2×2 box to remove single-point detections, then grow with a large $r = 25$ -pixel circular template to extend spot areas (including detected pores) beyond the horizontal-field super-penumbra.
- ii. 2: Masks 1-4 are added together and only pixels where all conditions are satisfied are selected.
- ii. 3: Mask 5 provides a negative-Boolean requirement, to remove not-dark but strong fields that can confuse the analysis.

The final masks included an additional identification of the polarity of B_z^h and location on the disk (latitude, longitude). Creating the plage masks without Mask 3, meaning without a filter on the local-component inclination angle, results in $\lesssim 5^\circ$ difference in, *e.g.* the mean and medians of the inclination angle distributions, by including non-radial points. As such, the interpretation of the bias may be systematically incorrect by a small amount, but avoiding having to resolve the 180° ambiguity may be advantageous in some situations.

2.2. Observational Data

2.2.1. *Hinode*/SpectroPolarimeter

We chose *Hinode*/SpectroPolarimeter (Kosugi et al., 2007; Tsuneta et al., 2008; Ichimoto et al., 2008; Lites et al., 2013) scans that follow NOAA AR 12457 (Table 1). The target scans include a small sunspot that does not fit our criteria for spot analysis, but does include a well-developed and minimally-evolving plage area (Figure 1). Standard Level-1, the calibrated spectra, and Level-2, the MERLINMilne-Eddington inversion results, were retrieved; Level 2.1 data were not used here, as we wanted to extend the disambiguation and ensure that it was consistent across inversion experiments (see section 2.2.3).

2.2.2. *Solar Dynamics Observatory*/ *Helioseismic and Magnetic Imager*

Data from the *Solar Dynamics Observatory*/ *Helioseismic and Magnetic Imager* (Pesnell, Thompson, and Chamberlin, 2012; Scherrer et al., 2012; Centeno et al.,

Table 1. Data / Target Summary

Target (Label)	Date/Time/ID	Location	Notes
Source: <i>Hinode</i> /SOT-SP		Cadence: 1/day	
AR12467	20151122_185049	N12 E42	HMI: 20151122_190000
"	20151123_181505	N12 E29	HMI: 20151123_182400
"	20151124_170005	N12 E16	HMI: 20151124_171200
"	20151125_154504	N12 E03	HMI: 20151125_160000
"	20151126_162004	N12 W10	HMI: 20151126_163600
"	20151127_151505	N12 W23	HMI: 20151127_152400
Source: <i>SDO</i> /HMI		Cadence: 96 m	
Spot 1 (Sp1)	2010.12.04 - 2010.12.12	N32	NOAA AR 11131
Plage 1 (Pl1)	"	"	Surrounding Spot 1
Plage 3 (Pl3)	"	S23	broad in longitude extent
Spot 2 (Sp2)	2016.05.17 - 2016.05.25	S07	NOAA AR 12546
Plage 2 (Pl2)	"	"	Surrounding Spot 2
Plage 4 North (Pl4N)	2016.05.13 - 2016.05.21	N07	
Plage 4 South (Pl4S)	"	S06	includes AR 12547

2014; Schou et al., 2012; Hoeksema et al., 2014) provide the known problematic data in this case, plus both time-series and full-disk data for testing inversion options and other mitigating procedures. To match the *Hinode*/SP data of AR 12457 we selected *SDO*/HMI segments close to the mid-times of the *Hinode*/SP scans (see Table 1) and extracted coincident FOV patches from the full-disk data (*not* as defined by the *SDO*/HMI Active Region Patch #6124's bounding boxes). The pipeline data included series `hmi.ME_720s_fd10` and `hmi.B_720s`, plus `hmi.S_720s` for some tests of inversions, and `hmi.lc_nolimbdark_720s` for continuum-feature identification.

Two additional time-periods were identified for study, targeting the presence of large, round, stable sunspots and well-distributed plage: 2010.12.04-2010.12.12 and 2016.05.13-2016.05.24 (Table 1). Not all analysis methods were available for the earlier time-period, but it was valuable to confirm behavior with a second large sunspot and additional plage areas. Custom-sized boxes were defined and extracted at the solar synodic rotation rate, to follow the targeted structures across the solar disk. In addition to the magnetic field-related segments, we utilized the confidence and the limb-darkened-corrected continuum intensity (as mentioned above). Context images for the targets selected from *SDO*/HMI time-series data are shown in Figures 2, 3, 4, 5.

2.2.3. Inversion Options

A number of different inversion options were evaluated, comprising two different groups of tests.

The first group used the Milne-Eddington inversion code developed for use with the NCAR/High Altitude Observatory Advanced Stokes Polarimeter (labeled ASP-ME; Skumanich and Lites, 1987; Lites and Skumanich, 1990; Leka, 1997) on *Hinode*/SP Level-1 data to systematically evaluate the impact of different implementation options. The options investigated include (see summary in Table 2):

- 1) optimization scheme: a genetic algorithm or least-squares minimization to obtain the global minimum of χ^2 fit between model atmosphere and observed spectra.
- 2) Fitting both 630.15, 630.25 nm lines or just the 630.25 nm. Different g_L factors imply different sensitivity to B but not ff , so multiple lines provide additional constraints.
- 3) Explicitly fitting for ff vs. explicitly setting $ff = 1.0$.
- 4) Weights assigned to $[I, Q, U, V]$: since the magnitude of the polarization signals in $[V]$ and $[Q, U]$ are of order $dI/d\lambda$ and $d^2I/d\lambda^2$ respectively and photon noise scales accordingly, in order to insure that the I does not dominate the χ^2 of the evaluation functions, weights $[w_I, w_Q = w_U, w_V]$ are usually a parameter supplied for the χ^2 calculation. We quote here $W_S^{\text{eff}} = W_s/\sigma_S$. Care must be taken when comparing codes and their parameter settings, as some request w_X while some refer to w_X^2 .

The second group compares different inversion codes that may differ in a variety of ways. The different codes are tested on one or both of *SDO*/HMI `hmi.S.720s` polarization images or *Hinode*/SP Level-1 spectra, as listed in Table 3. The different systems tested include:

- The pipeline *Hinode*/SP Level-2 output from the MERLIN Milne-Eddington code (heredity from ASP-ME).
- The pipeline output from the Very Fast Inversion of Stokes Vectors (VFISV Borrero et al., 2010; Centeno et al., 2014) from the `hmi.ME.720s_fd10` series.
- The UNNOFit code (Bommier et al., 2007) was applied only to the AR 12457 targets, but with both *Hinode*/SP Level-1 data and *SDO*/HMI `hmi.S.720s` data as input. UNNOFit introduced the magnetic filling factor as a free parameter of the Milne-Eddington inversion. All free parameters describing the non-magnetic part of the atmosphere are set to equal those of the magnetic part, except for the magnetic field vector itself. This procedure was recently implemented in a new VFISV inversion (see next point), with a slight difference in the series of the eight other parameters, where UNNOFit also determines the Voigt parameter a and eliminates the source function at the photosphere base by normalization. UNNOFit was the first code that explicitly allowed a variable atmosphere for the non-magnetic component, although it is set to be identical to the atmosphere of the magnetic component. However, Bommier et al. (2007) also showed that nine parameters can exceed the information content of the spectra as needed for a successful inversion, and that only the pixel-averaged average magnetic field strength $ff * B$ is finally determined.

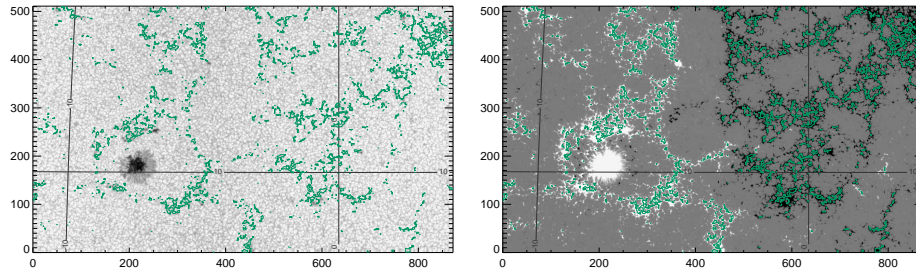


Figure 1. *Hinode*/SP “normal” scan of AR 12457, ID 20151124_170005, showing (left) continuum (scaled to $1.1 \times \text{median}(I_c)$) with latitude/longitude contours, and (right) B_z^h . Plage points are identified (green contours). All target image axes are simply in pixel numbers.

- A new version of the Very Fast Inversion of Stokes Vector (VFISV_ABGM; Borrero et al., 2010; Grignon-Marín et al., 2021) was developed for implementation with *SDO*/HMI data to explicitly include a fit for the fill fraction. Similar in the approach to UNNOFit (see above), it should be noted that the Voigt parameter is fixed at $a = 0.5$ and the source function at the base of the photosphere is a fitted parameter. The results from this inversion have been shown to mitigate the bias Grignon-Marín et al. (2021); Liu et al. (2022). One difference between the VFISV_ABGM data used here and that presented in Grignon-Marín et al. (2021); Liu et al. (2022) is that we used no polarization threshold for the inversion whereas a threshold of 0.25% was used in those cited works. We removed the polarization threshold in order to ensure no discontinuity near weak-signal plage areas. No additional scattered light correction was performed.
- The SynthIA approach is not really an inversion *per se*, it is a Convolutional Neural Network that has been trained on the *Hinode*/SP Level-2 output with *SDO*/HMI `hmi.S_720s` polarization images as input (Higgins et al., 2021, 2022). The full-disk results provide field and fill-fraction separately, with an overall fidelity closer to *Hinode*/SP pipeline output than *SDO*/HMI pipeline output.

We additionally test the question of polarization noise. As briefly demonstrated in (Pevtsov et al., 2021), noise in the linear polarization $[Q, U]$ signals contribute to the bias. We conduct tests comparing inversions using input spectra from the *SDO*/HMI `hmi.S_720s` series to those using input spectra from the `hmi.S_5760s` series, which are 96 m integrated Stokes spectra, and demonstrably lower in random (photon) noise.

Not all possible permutations were executed, but a sufficient number with sufficient range of options so as to quantitatively judge the impact of the different approaches to the bias. The tests are summarized in Tables 2, 3; please note the method monikers will be used in later discussion and figures.

2.2.4. Disambiguation

The data from all inversions of both *Hinode*/SP and *SDO*/HMI data are inherently 180° ambiguous in the plane-of-the-sky component. All inverted data

Table 2. Tests Run on *Hinode*/SP target AR 12457

Line(s) (nm)	<i>ff</i> fit explicitly?	Optimization method	W_S^{eff} [I, Q&U, V]	Moniker	Notes
Data Source: <i>Hinode</i> /SP; Inversion: ASP-ME ¹					
630.15, .25	✓	Genetic	[1,10,3.2]	A-DEF	“Default”
630.15, .25	✓	Genetic	[1,31.2,3.2]	Aw1	weights-test #1
630.15, .25	✓	Least-Squares	[1,31.2,3.2]	ALSw1	
630.15, .25	✓	Genetic	[1,10,2.2]	Aw2	weights-test #2
630.15, .25	✓	Least-Squares	[1,10,2.2]	ALSw2	
630.15, .25	✓	Genetic	[1,1,1]	Aw3	weights-test #3
630.15, .25	✓	Genetic	[1,3.2,3.2]	Aw4	weights-test #4
630.15, .25	✓	Least-Squares	[1,10,3.2]	ALS	
630.25	✓	Genetic	[1,10,3.2]	A1	
630.25	✓	Genetic	[1,31.2,3.2]	A1w1	
630.25	✓	Genetic	[1,10,2.2]	A1w2	
630.25	✓	Least-Squares	[1,10,3.2]	A1LS	
630.25	X	Genetic	[1,10,2.2]	A1NFw2	
630.25	X	Genetic	[1,10,3.2]	A1NF	
630.25	X	Least-Squares	[1,10,3.2]	A1NFLS	
630.15, .25	X	Genetic	[1,10,2.2]	ANFw2	
630.15, .25	X	Genetic	[1,10,3.2]	ANF	
630.15, .25	X	Least-Squares	[1,10,3.2]	ANFLS	
Data Source: <i>Hinode</i> /SP; Inversion: OTHER					
630.[15,.25]	✓	LM ²	[0.01,1,0.1]	MERLIN	L2 pipeline ³
630.15	✓	LM	[1,1,1]	UnnoFit_6301	UNNOFit ⁴
630.25	✓	LM	[1,1,1]	UnnoFit_6302	UNNOFit
Data Source: <i>SDO</i> /HMI; Inversion: VFISV					
617.3	X	LM	[1,3,2]	PIPE	hmi.ME_720s_fd10 ⁵
617.3	✓	LM	[1,3,2]	ABGM	su_abgm ⁶
Data Source: <i>SDO</i> /HMI; Inversion: OTHER					
617.3	✓	CNN	n/a	SynthIA	CNN ⁷
617.3	✓	LM	[1,1,1]	UnnoFit_HMI	UNNOFit

1: Skumanich and Lites (1987); Leka (1997)

2: Levenberg-Marquardt (LM) minimization algorithm (see Press et al., 1992)

3: <https://sot.lmsal.com/data/sot/level2d/>

4: Bommier et al. (2007)

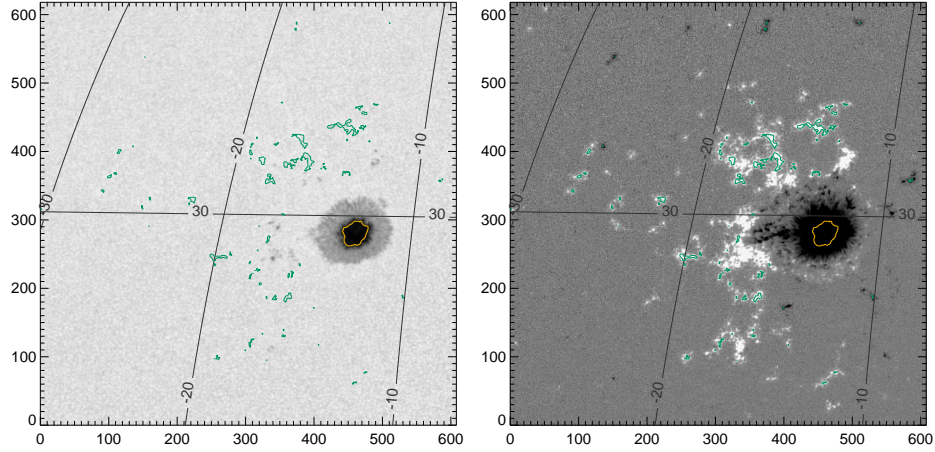
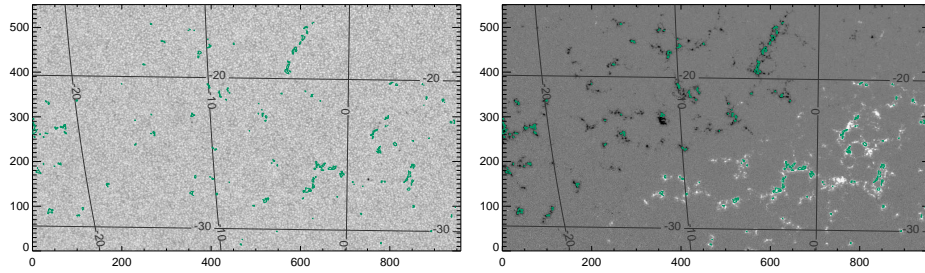
5: Centeno et al. (2014)

6: Griñón-Marín et al. (2021)

7: Higgins et al. (2021, 2022)

Table 3. Tests Run on *SDO*/HMI Multi-Day TimeSeries Targets

<i>ff</i> Fit?	Optimization	Moniker	Notes
2010.12.04_05:48:00 – 2010.12.12_04:12:00: Spot #1, Plage #1, Plage #3			
X	LM	PIPE	<i>SDO</i> /HMI pipeline
✓	LM	ABGM	<i>su_abgm</i>
✓	CNN	SynthIA	SynthIA CNN
2016.05.13_20:48:00 – 2016.05.24_19:12:00: Spot #2, Plage #2, Plage #4			
X	LM	PIPE	<i>SDO</i> /HMI pipeline
X	LM	PIPE_5760	Input: <i>hmi.S_5760s</i>
✓	LM	ABGM	<i>su_abgm</i>
✓	LM	ABGM_5760	Input: <i>hmi.S_5760s</i> , <i>su_abgm</i>
✓	CNN	SynthIA	SynthIA CNN

**Figure 2.** Target sunspot “Spot 1”, NOAAAR 11131 that transited the disk 2010.12.04 - 2010.12.12, at N30, shown here at 2010.12.07_07:24:00.TAI. The surrounding plage is “Plage 1”. Left: Continuum, Stonyhurst grid, with axes indicating pixels. Right: B_z^h from the Minimum-Energy disambiguation (see Section 2.2.4), same Stonyhurst grid, with contours of selected plage points (green) and center-spot radial-field area (yellow).**Figure 3.** Same as Figure 2 but for “Plage 3” that transited 2010.12.04 - 2010.12.12, almost directly south of NOAAAR 11131 centered at S25, shown here at 2010.12.07_20:12:00.TAI.

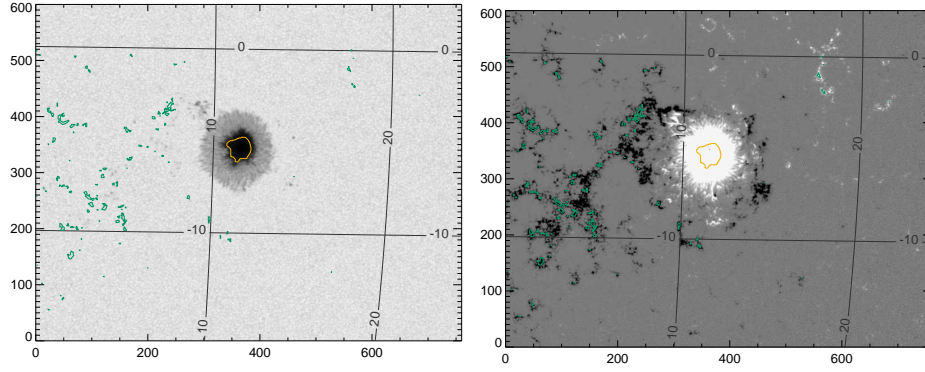


Figure 4. Same as Figure 2 but for “Spot 2”, NOAA AR 12546, and accompanying “Plage 2” that transited the disk 2016.05.14 - 2016.05.25, shown here at 2016.05.21_06:24:00_TAI.

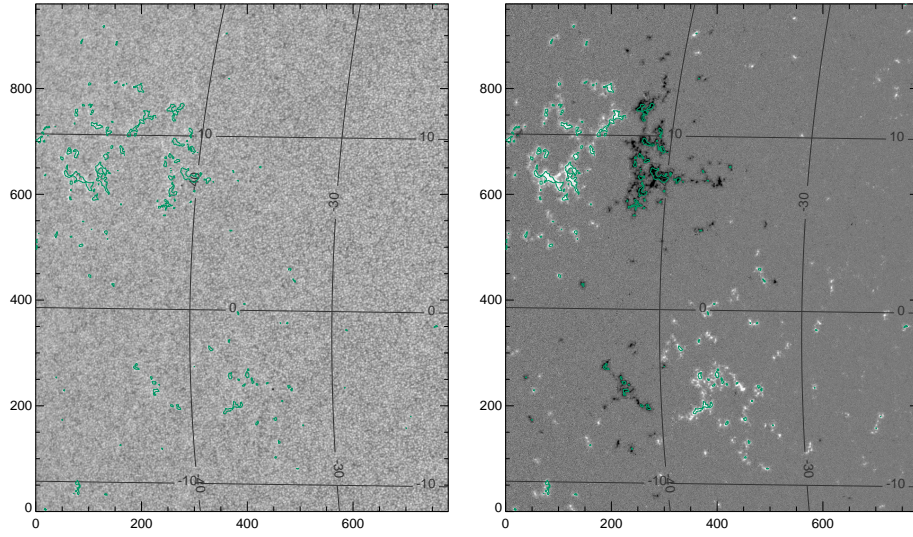


Figure 5. Same as Figure 2 for target plage area “Plage 4” which transited the disk 2016.05.13 - 2016.05.21, shown at 2016.05.14_08:00:00_TAI. Of note, this region was divided into “Plage 4 North” and “Plage 4 South” for analysis. Plage 4 South eventually produced sunspots and was labeled NOAA AR 12547, but the sunspot points are excluded for plage analysis.

that were compared using the local components were disambiguated using the “minimum-energy” method (ME0; Metcalf, 1994; Leka, Barnes, and Crouch, 2009; Hoeksema et al., 2014, available at www.nwra.com/AMBIG) with a cooling schedule that generally matched both *SDO*/HMI and the *Hinode*/SP Level2.1 data products: `tfactr`=0.98, `neq`=100. The primary difference in how ME0 was called relative to the *SDO*/HMI pipeline concerns a lower `[athresh, bthres]`=`[95,100]` to capture more near-plage areas, and deploying the spherical option for the larger-FOV *SDO*/HMI data. The local components were computed then using planar or spherical geometry, accordingly.

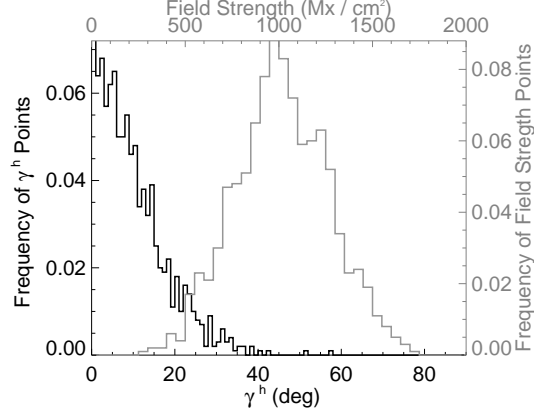


Figure 6. Distributions of heliographic or local inclination angle γ^h (black) and field strength (grey) for the “plage-like” distributions in the model. $\gamma = 0$ is radially-directed (opposite gravity). These 1000-point samples were then placed across a variety of viewing angles.

2.3. Model Data

To complement the analysis of observational data, model data were constructed with which to test the hypotheses and the mitigation strategies. On a latitude / longitude grid ranging in both directions $\pm 80^\circ$ in 2.5° increments, 1,000-point samples were generated to mimic expected distributions of plage: the radial component is a normally-distributed random sample centered at 1,000G with a standard deviation of 250G, the horizontal component was a normal distribution, standard deviation 200G; the azimuthal angle was a uniform distribution across 2π (Figure 6). Only $B_z^h > 0$ positively-polarity “plage” was considered here.

From this grid, coordinate transforms re-create the image-plane components $|\mathbf{B}|, \gamma^i, \alpha^i$ or alternatively B_x^i, B_y^i, B_z^i , the last being B_{\parallel} and $B_{\perp} = \sqrt{B_x^i{}^2 + B_y^i{}^2}$. Noise was optionally added at ‘low’, ‘medium’, and ‘high’ levels: a normal-distribution random sample with $\sigma = [5, 10, 50]$ G for B_{\parallel} was paired with a normal distribution with $\sigma = [100, 200, 300]$ G for B_{\perp} , although the absolute value was added (since the effective photon noise for total linear polarization is positive-definite, see discussion in Pevtsov et al. (2021)). The noise in azimuthal angle was a normal distribution with standard deviation approximately $[2, 4, 6]^\circ$. In an attempt to mimic the noise maps of *SDO*/HMI (see Hoeksema et al., 2014, their Figure 7), we tested adding noise at the levels listed above but scaled as $1.0/\sqrt{\mu}$ such that the noise increases near the limb, but this made little difference in the final outcomes. No attempt was made to model the impact of unresolved field or incorrect fill factor (although see Leka and Barnes, 2012).

2.4. Analysis and Metrics

Simply detecting a “sign flip” in a re-binned image of a local heliographic field component as a plage area transits the central meridian is a useful initial

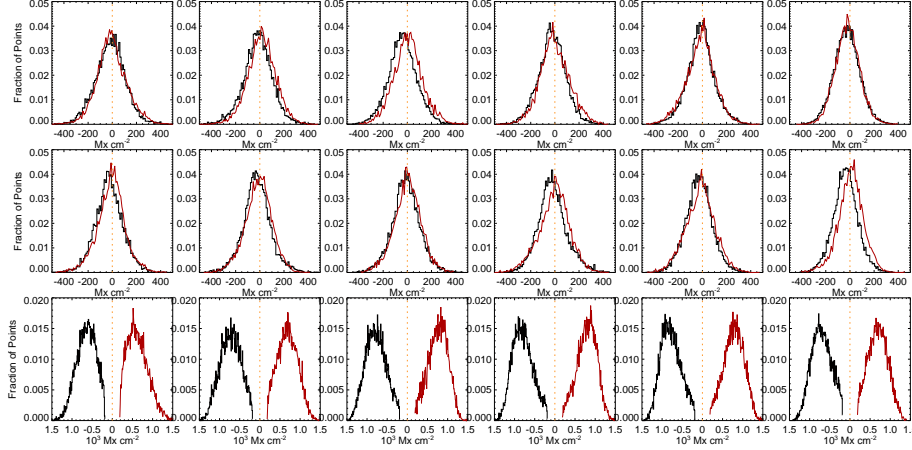


Figure 7. Histograms of plage-identified areas of NOAA AR12457 for the *Hinode*/SP Level-2 pipeline data output, prepared as described in the text. Left to Right: results from the six scans (Table 1); central meridian crossing is at approximately 2015.11.25 00:00, between the 3rd and 4th scan. Red/Black indicate pixels that have positive/negative B_z^h ; histograms are for B_x^h (top), B_y^h (middle), and B_z^h (bottom). While there is some variation, the distributions for B_x^h and B_y^h are essentially independent of polarity and location on the disk.

diagnostic (Pevtsov et al., 2021; Liu et al., 2022). However, it is difficult to quantitatively evaluate the bias in this manner (*c.f.* (Rudenko and Dmitrienko, 2018)), or determine its full impact.

We develop quantitative metrics based on the believed physical characteristics of solar structures in order to evaluate the bias. In some cases, temporal sampling is mapped to spatial sampling, again relying on the physical and statistical qualities of plage in that the distributions of the underlying fields are not expected to evolve significantly over the course of a few days.

2.4.1. Distributions of B_x^h , B_y^h , B_z^h with Central Meridian Distance and Observing Angle

Similar to Figure 4 in Pevtsov et al. (2021), histograms of the heliographic B_x^h are presented separately for pixels with $\pm B_z^h$. Without the presence of filament channels, nearby large active regions or other phenomena that could introduce a physical direction preference, the assumption is that the histograms should overlap: the distribution of B_x^h or B_y^h should not differ according to either the sign of B_z^h or viewing angle. Tracking the plage in NOAA AR12457 over 6 days, we see the very different behavior between the *Hinode*/SP pipeline output (Figure 7) and the *SDO*/HMI pipeline output (Figure 8), with consistent $\langle B_x^h \rangle$ and $\langle B_y^h \rangle$ regardless of polarity and viewing angle for the former, and a switch of $\langle B_x^h \rangle$ between east/west hemisphere for the latter, as well as a consistent offset in $\langle B_y^h \rangle$.

In situations such as NOAA AR12457 where there is a sufficient sample of plage with both polarities, the behavior is summarized by metrics describing

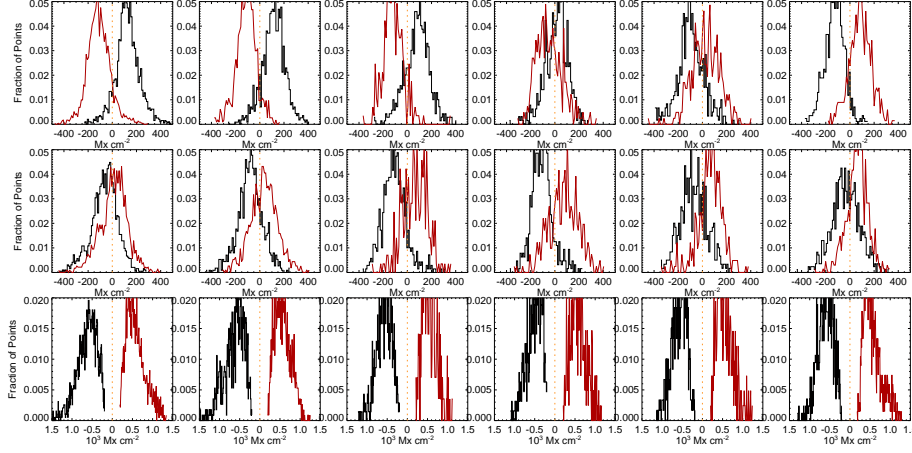


Figure 8. Same presentation as in Figure 7 and for the the same field of view, but from *SDO*/HMI pipeline data, prepared as described in the text. Note the switch of the B_x^h histogram peaks as the regions transits the central meridian, and the sustained but consistent difference in B_y^h .

the differences in the distributions of target magnetic components. Specifically, metrics should target the behavior of the B_x^h and of B_y^h most notably, plus B_z^h when it provides information. The absolute separation $|\text{sep}|$ is the absolute difference of the medians of two distributions of the target $B_x^h, B_y^h, \text{ or } B_z^h$, the two distributions being whether the underlying field has $B_z^h > 0$ or $B_z^h < 0$; the mean absolute separation is taken over the 6 samples. This is accompanied by the standard deviation of the *signed* separation, $\sigma(\text{sep})$ which is larger for a switch in sign and smaller if, for example, the distributions are separated but do not change significantly between samples. We additionally consider the median absolute deviation (MAD; $\text{med}(|\hat{X} - \bar{X}|)$, where \hat{X} is the median (most probable) value for the target distribution) and \bar{X} is its median over the 6 samples, and the maximum absolute deviation MaxAD which is the maximum difference between the median of the target distribution (separately for $B_z^h > 0$ or $B_z^h < 0$) from its expected value: 0.0 for B_x^h and B_y^h and the mean B_z^h over the 6 samples, as we hypothesize little evolution.

This analysis is also applied to the sub-area targeted patches of *SDO*/HMI time-series data. In Figures 9 and 10 we summarize the behavior of the target distributions as a function of the mid-point longitude for all three vector components. Quantitative summaries take the same form as for the NOAA AR 12457 analysis: mean absolute separation, standard deviation of the signed separation, MAD, and MaxAD.

2.4.2. Distributions of $|\gamma^i|$ with Observing Angle

Ideally there should be metrics available from the image-plane components themselves, without requiring the disambiguation step. If we describe the bias as an over- (or under-) estimate in the B_{\perp} component, then this will manifest in the

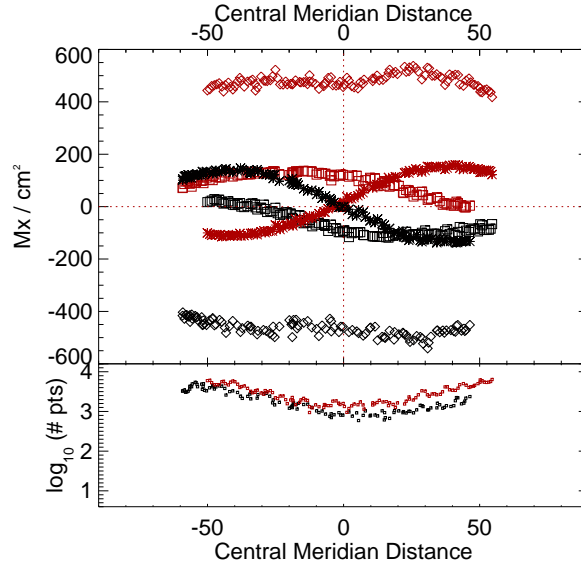


Figure 9. Timeseries of means of the distributions of $B_x^h(*)$, $B_y^h(\square)$, $B_z^h(\diamond)$ for plage-identified concentrations in “Plage 3” (see Fig. 3) and the standard *SDO*/HMI pipeline (“PIPE_720s”) output, plus the number of points in the distributions (subplot). Red/black indicate positive/negative polarity B_z^h .

image-plane inclination angle γ^i . It is in this context that focusing on plage and the radially-oriented locations within stable sunspots becomes useful, because we can assume that for radially-directed fields, $B_r = B_{\parallel}/\mu$, where $\mu = \cos(\theta)$ the cosine of the observing angle (Svalgaard, Duvall, and Scherrer, 1978; Wang and Sheeley, 1992). In other words, for radially-directed fields without bias, $\gamma^i = \mu$.

First we examine the heliographic (local, or physical) inclination angle of the target plage points in the NOAA AR 12457 data and confirm that the distributions are the same between the positive and negative regions, change minimally as a function of east/west location, and while not exactly radial, are not particularly inclined (Figures 11, 12, top panels).

The distribution of $|\gamma^i|$, however, distinctly changes shape as a function of observing angle, and differs between *e.g.* the *SDO*/HMI and *Hinode*/SP pipeline output (Figures 11, 12, lower panels). The skew of the distributions shows exactly opposite behavior with east/west location between the two pipeline data outputs.

Figures 11, 12 (top panels) confirm that there is a distribution of orientations within these structures, of course, but they are dominated by radially-directed field. Hence we focus on $E(\gamma^i)$, the expected value or most probable value, and whether it tracks the observing angle $\mu = \cos(\theta)$ (Figure 13). The degree to which $E(\gamma^i)$ points *vs.* θ lie off the $x = y$ line provides information on the bias, including whether there is an under- or over- estimation of B_{\perp} . This key diagnostic can be performed on limited-FOV time-series data for (statistically) unchanging structures, but can also be used for full-disk data without requiring any time-series, provided the required structures are present.

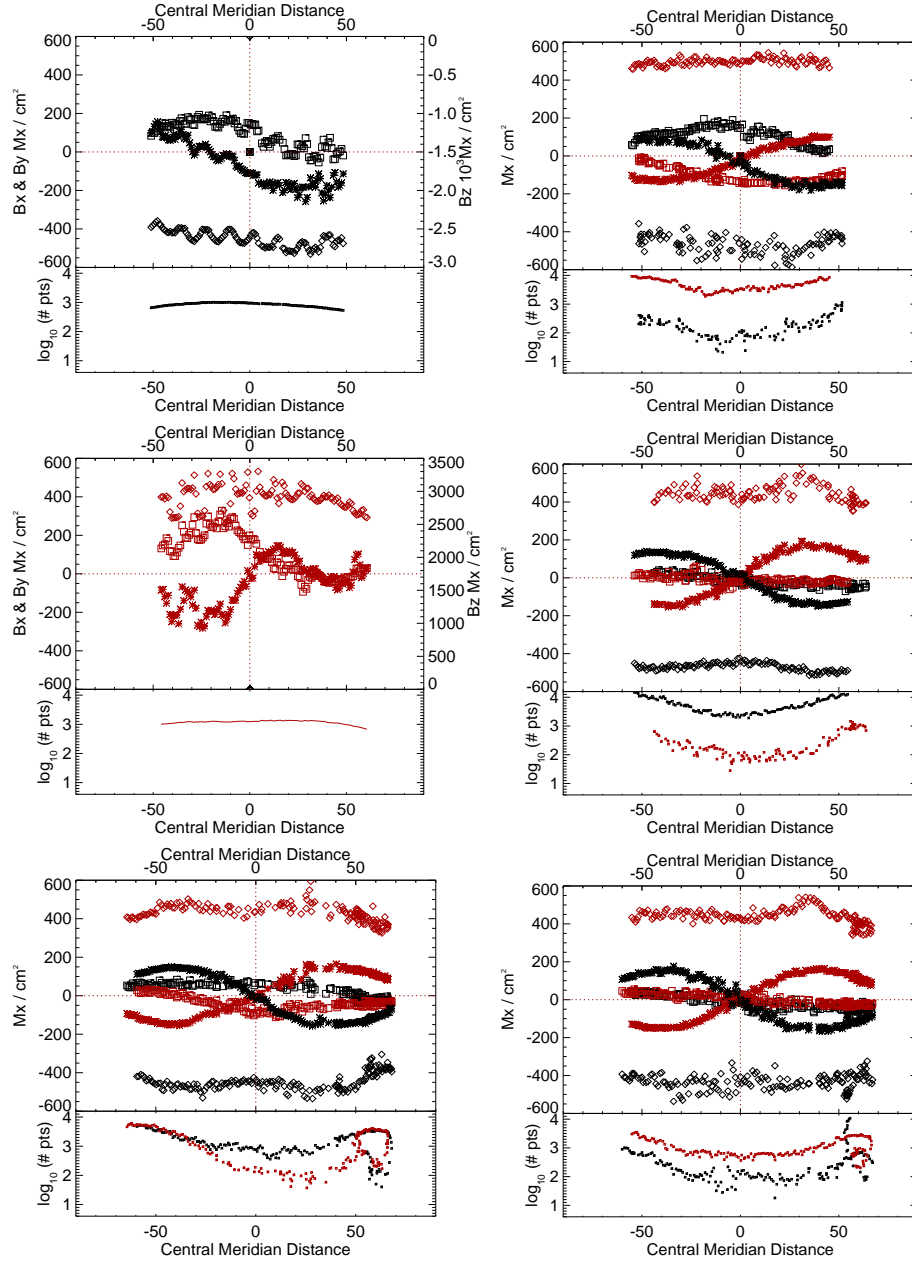


Figure 10. Same presentation as Fig. 9: B_x^h (*), B_y^h (\square), B_z^h (\diamond), Red/black indicate positive/negative polarity B_z^h . (Top, left/right): Spot 1, Plate 1, (Middle, left/right): Spot 2, Plate 2, (Bottom, left/right) Plate 4 North, Plate 4 South. For the spot-related plots, note the different scale (right-hand y-axis) for the B_z^h component.

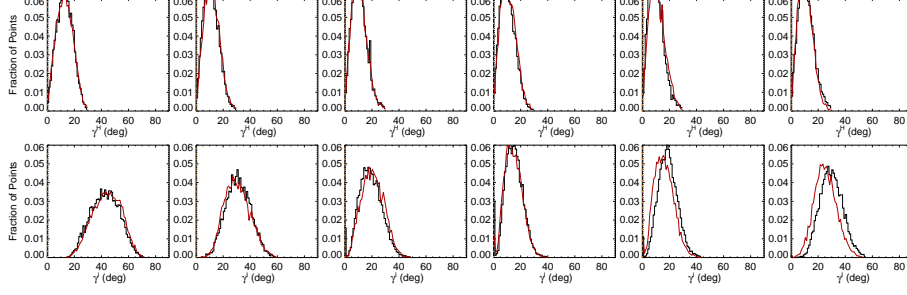


Figure 11. Same presentation as in Figure 7 for *Hinode*/SP MERLIN pipeline output data, but showing the distribution of γ^h (top) and γ^i (bottom).

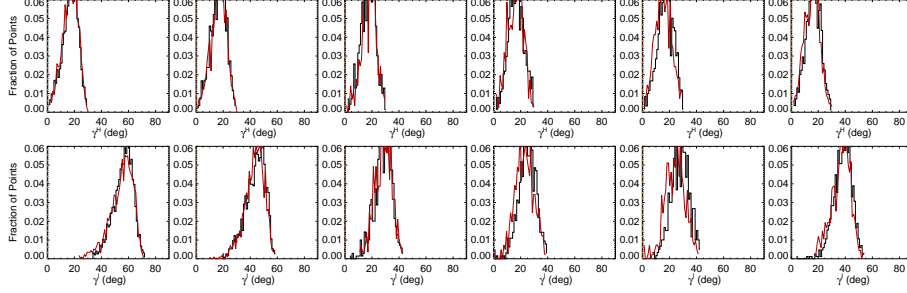


Figure 12. Same general presentation as Figure 8 for *SDO*/HMI pipeline VFISV output data, but showing the distribution of γ^h (top) and γ^i (bottom) as per Figure 11.

In Figure 13, we see that the MERLIN $E(\gamma^i)$ vs. θ results align with $x = y$ nearly perfectly, while the three examples from the *SDO*/HMI pipeline all show significant deviations, although with inconsistent functional form. The differences between the two plage-targeted examples could be due to different observing epochs (2010 *vs.* 2016), or subtle changes in the tracked structures due to evolution or field-of-view. The deviation from $x = y$ for the sunspot confirms the presence of the bias in structures that have strong, pixel-filled signal, presumably with $ff = 1.0$. The different form of $E(\gamma^i)$ vs. θ for the spot target compared to plage targets may be due to a combination of signal/noise ratio, signal saturation, scattered light treatment, plus the different impact of bias according to the treatment of ff .

The primary metric then to evaluate $|\gamma^i|$ distributions for plage as a function of $\mu = \cos(\theta)$ is the Gini coefficient \mathcal{G} or Receiver (Relative) Operating Characteristic (ROC) Skill Score (ROCSS; Jolliffe and Stephenson, 2012; Leka, Barnes, and Wagner, 2018) $\mathcal{G} = 2 * \text{AUC} - 1$, where the AUC metric is the integrated area under the curve. Provided sufficient coverage in μ is available, \mathcal{G} essentially measures a signed area departure from the $x = y$ line. Other metrics such as the the maximum absolute deviation could also be used here, but \mathcal{G} is intuitive, for $\mathcal{G} > 0$ indicates over-estimation of B_{\perp} whereas $\mathcal{G} < 0$ indicates an underestimation. To compute \mathcal{G} , we normalize the ranges to $[0, 1]$ and extend the sampled ranges to those ends for all data, in order to cursorily account for

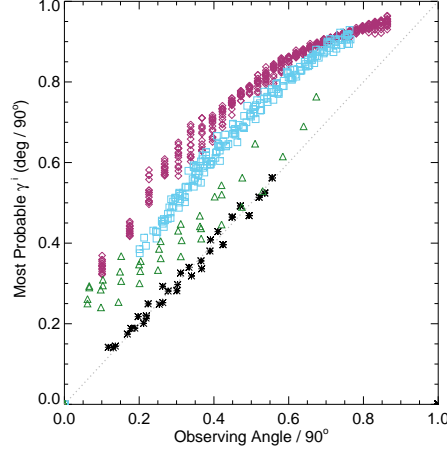


Figure 13. Plot of the most probable image-plane absolute inclination $|\gamma^i|$ (y-axis) for plage areas in rings or bins of $\Delta\mu = 0.025$ as a function of the central value for that ring (x-axis); both axes are in degrees but normalized by 90° . Shown are *Hinode*/SP MERLIN Level-2.0 data for NOAA AR 12457 for all days sampled (black *), and three targets from the *SDO*/HMI VFISV pipeline: full-disk data for 2016.05.18 (red \diamond), “Plage #3” (blue \square), and “Spot #2” (green \triangle). Dashed line: $x = y$. The *SDO*/HMI full-disk data are sampled for 24hr at 96 m cadence (15 samples) and show as well the OBS_VR-related variation (Hoeksema et al., 2014; Schuck et al., 2016).

different sampling in $\mu = \cos(\theta)$ between datasets and tests. The choice of using angles in degrees but normalized by 90 simply provides an intuitive presentation and AUC calculation; the same information is available using μ and $\cos(|\tilde{\gamma}^i|)$, similarly both normalized to $[0, 1]$.

3. Results

There are a large number of tests that were performed; here we summarize results for targeted questions, first the experiments with model data, then observational.

3.1. The Magnitude and Impact of the Problem

The most obvious impact of this bias manifests in the sign-flip of B_x^h as extended patches of unresolved structures rotate east/west across the solar disk, as described here and in previous papers (Pevtsov et al., 2021; Liu et al., 2022). The magnitude is demonstrated here quantitatively (Figures 8, 9, 10): up to a few $\times 100 \text{ Mx cm}^{-2}$ signal of bias is present, or almost 30% of the total pixel-averaged field magnitude for the plage regions.

It was surmised in those papers that there should be a bias in the north/south distribution of B_y^h as well. It is shown quantitatively here (same figures). The B_y^h component behaves in an opposite way for plage points with $B_r > 0$ vs. $B_r < 0$ when located north vs. south of the equator. The effect is somewhat subtle due to the limited north/south extent available for analysis, but it is clear.

It was also briefly mentioned in previous papers that there may be an impact on the inferred radial component B_z^h or B_r (the component most widely used for global modeling presently), and this is also demonstrated here. It is a smaller effect still, but can be seen as subtle peaks in the most probable pixel-averaged flux away from disk center, and a dip in the magnitude near disk center.

In summary, because this is a problem in image plane, it impacts all vector components in physical space, including B_r (B_z^h). It will also lead to incorrect or biased estimates of any derived quantity such as the vertical current, the force-free parameter α , *etc.* The bias is strongest in *unresolved* structures – and as such will constitute significant portions of active regions as well as the large-scale plage regions.

It was stated in the earlier papers that there was no bias in the strong-field or $ff \approx 1.0$ areas. We find this is not actually the case. We show that in the central portions of two large, round, stable sunspots, there is a non-zero most probable inclination. The direction and magnitude of the most-probable magnetic field vector changes sign (or nearly changes sign) for B_x^h as the spots transit the central meridian, and displays a non-zero difference in the most probable value of B_y^h as well. The variations in B_z^h are smaller than the orbital-velocity related variations and cannot be confirmed here.

The bias in $ff \approx 1.0$ areas may be caused ultimately by unresolved field or the detailed handling of scattered instrumental light (LaBonte, 2004). It indeed fails to cause a full sign reversal of the components, that is true. However we disagree with Liu et al. (2022) that “This bias does not occur in strong field regions in sunspots.” The signature of the bias is present, but only apparent with a quantitative examination of the field-component distributions.

3.2. Results from Model Data Experiments

The simple toy model of plage-like distribution of field across a range of observing angles is used to test three possible contributing bias distributions: (1) a constant magnitude of bias added to B_\perp , (2) a contribution to B_\perp that is a function of total field, and (3) a contribution to B_\perp that is a function of observing angle, mimicking that which would be expected with systematically higher fill factor derived in regions away from disk center (hence the bias introduced by an imposed $ff = 1.0$ will be greater toward disk center). The goal here is to reproduce some of the quantitative characteristics observed: the changing skew of γ^i distributions with observing angle, confirm the behavior of the Gini coefficient with bias and its sign, and understand the source of the sometimes-observed curvature of γ^i as a function of observing angle (Figure 13). In most cases, both positive and negative bias is added.

The distributions of $|\gamma^i|$ with observing angle show a general trend as is seen in the *Hinode*/SP data (see Figure 11) of a changing shape with observing angle (Figure 14, Top). The changes are indeed influenced by the degree of photon noise present.

Tracking this change in skew as a function of the experiments performed regarding noise and bias is shown in Figure 14, Bottom. There is a distinct form of the change in skew of the $|\gamma^i|$ distribution as a function of viewing

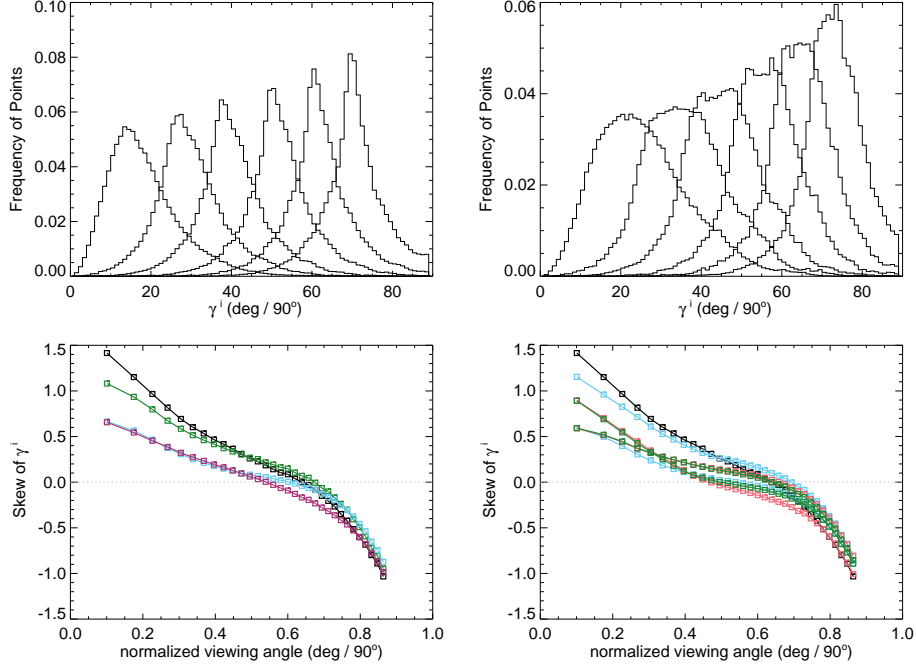


Figure 14. Top: histograms of the “observed” $|\gamma^i|$ of the model data for bins that are 0.025-wide centered at $\mu = [0.3625, 0.50125, 0.6625, 0.8125, 0.9125, 0.9875]$. (Left): “low-noise” case, (Right): “high noise” case. **Bottom:** The skew of the $|\gamma^i|$ distributions as a function of viewing angle as the result of different experiments. (Left): effect of different levels of photon noise, no additional bias added. Black Squares: no noise at all; also shown are “low noise” (green), “medium noise” (light blue) and “high noise” (red). (Right): tests of different characterization of bias are shown, as related to the same Black squares (no noise or bias). Red: the experiment (1), a constant magnitude of bias at ± 200 added to B_{\perp} ; Light Blue: (2), a bias that is $\pm 25\%$ of the total field strength; Green: (3) a bias of $\pm 200 \times \mu$.

angle, without any additional noise. The addition of photon noise and bias that originates with according to the three experiments present departures from the no-noise case. However, the ‘optimal’ curve (the no-noise no-bias case) is not straightforward to describe: it is not a simple function of observing angle. The curves with added noise and bias depart from the optimal, but in sometimes subtle and non-unique ways. As such, we elect to not use the skew of the $|\gamma^i|$ distributions as a quantitative test of bias in the observational data.

The behaviors of the “observed” $E(|\gamma^i|)$ with viewing angle as per experiments with bias are shown in Figure 15 (panels (a)-(c) and for photon noise only (panel (d)). The ‘optimal’ situation of no photon noise and no bias is the $x = y$ line. Similar to above, the addition of bias produces deviations from the ideal case but for the bias cases (panels (a)-(c)) the only unique signature is the spread at large viewing angle, and a slight difference in shape. To summarize the performance when both bias and noise are included, we present Figure 16 where we focus on the Gini coefficient \mathcal{G} as the bias levels are varied. The black “no noise” cases will reflect the curves in Figure 15 (a)-(c), the other curves are as labeled. The

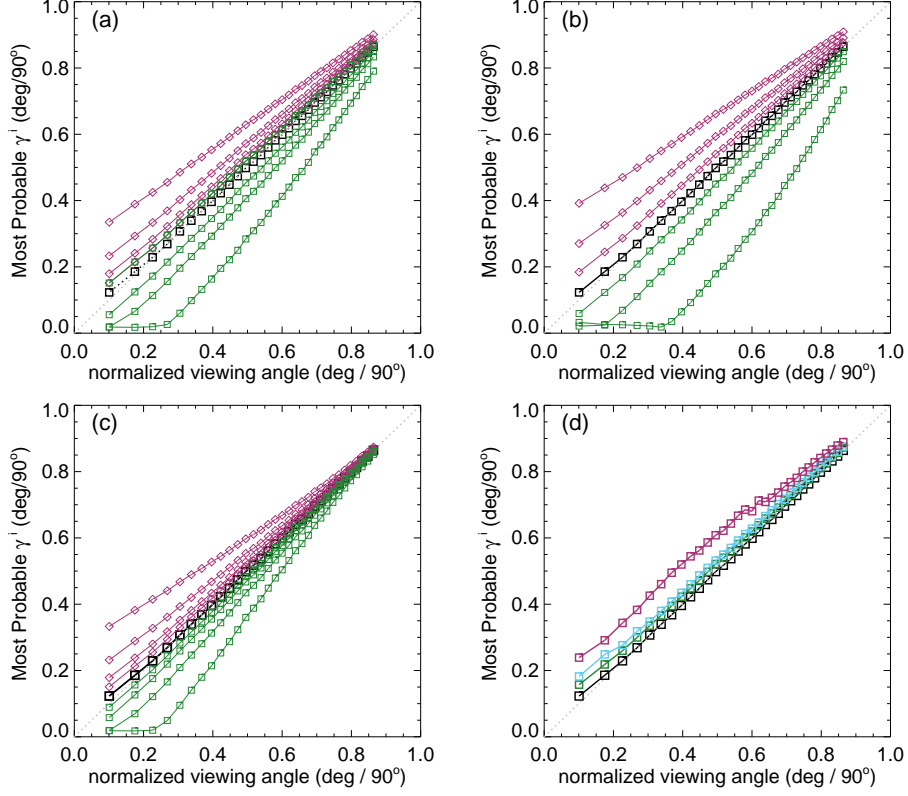


Figure 15. Results of model tests, demonstrating just one approach at a time and its behavior. For each, the black boxes are ‘no noise, no bias’ results for reference. (a) Experiment (1): no noise, constant B_{\perp} bias at $\pm 50, 100, 200, 400 \text{ Mx cm}^{-2}$ (red diamonds/green squares); (b) Experiment (2): no noise, B_{\perp} bias at $\pm 10, 25, 50\%$ (red diamonds/green squares) of total field; (c) Experiment (3): no noise, B_{\perp} bias is added at levels $\pm[50, 100, 200, 400] * \mu$ (red diamonds/green squares); (d) Magnetogram noise only is added (no additional bias) for B_{\parallel}, B_{\perp} respectively at the $[0, 0]$ (‘no noise’, black), $[5, 100]$ (‘low noise’, green), $[10, 200]$ (‘medium noise’, light blue) and $[50, 300]$ (‘high noise’, red) levels (see text). For all, the $x = y$ line is indicated.

impact of including both noise and bias is to increase the departure from $\mathcal{G} = 0$ overall and bring even negative bias toward $\mathcal{G} > 0$. The latter effect is caused by effectively a “canceling out” effect between the bias and the noise. Given the noise levels in *SDO*/HMI data are roughly between the “Mid Noise” and “High Noise” cases, we can possibly use these plots to rule out some extreme cases, but the curves and behaviors are similar enough to probably preclude determining a functional form of the bias.

We find that the impacts of over- or under-estimating B_{\perp} do not always manifest symmetrically about the $x = y$ line for the $E(|\gamma^i|)$ vs. μ relation. And while the shapes of the curves deviate slightly from linear as both photon noise and bias are added, we are unable with this toy model to replicate the curvature observed in the *SDO*/HMI pipeline output (Fig. 13), even when testing a bias whose behavior is a function of observing angle, as expected by errors in fill frac-

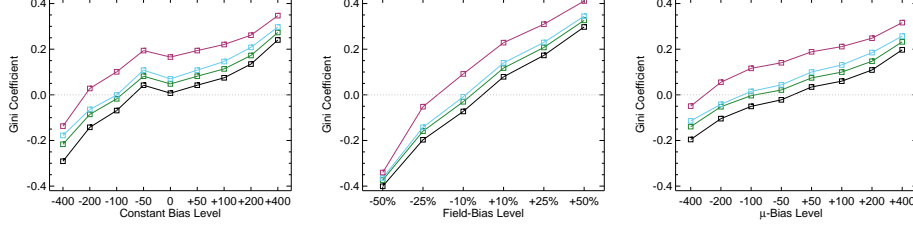


Figure 16. Summary statistics (Gini coefficients \mathcal{G}) for the toy-model experiments, here including the behavior of the cross-purpose noise and bias combinations (*e.g.* adding bias and photon noise, both). Left: Experiment (1): “constant Bias Level” applied, Middle: Experiment (2): the bias as a fraction of the total field strength, Right: Experiment (3): bias level that is then multiplied by $\mu = \cos(\theta)$ for a model of the effect of mis-representing ff . Colors indicate photon noise levels: Black: “No Noise”, Green: “Low Noise”, Light Blue: “Mid Noise”, Red: “High Noise”.

tion. The $E(|\gamma^i|)$ *vs.* μ behavior of Spot #2 is less curved, and closer to the curves produced by the toy model with moderate levels of positive bias. The difference in the $E(|\gamma^i|)$ *vs.* μ behavior (curved *vs.* closer to linear) between the Spot #2 and the plage points in Figure 13 is thus likely due to unresolved structures and hence non-unity ff in the latter, and how that manifests with observing angle. Further model development to investigate the impact of unresolved structure is beyond the scope of this paper (although see the approach in Leka and Barnes, 2012).

3.3. Results from Testing Mitigation Approaches

As discussed in Section 2.2.3, there are other aspects of interpreting specropolarimetric signals that can lead to differences in inferred flux densities. The results of our tests are summarized in Figures 17, 18, and 19, and then in Figures 20, 21, and 22, using the quantitative evaluation metrics on both image-plane $|\gamma^i|$ and heliographic B_x^h, B_y^h, B_z^h components (see Sections 2.4.1, 2.4.2). While the latter indeed rely on the resolution of the 180° ambiguity in the B_{\perp} component, the same method was applied throughout, addressing one point in Sainz Dalda (2017). The \mathcal{G} can be positive or negative, all other metrics are positive; all metrics used here tend to zero for best performance (less bias). For all metrics evaluated on time-series data, there may be evolution or field-of-view departures that result in non-zero metrics, but all of the methods are evaluated on consistent data, so comparisons between methods as grouped here are valid.

From the analysis of the AR 12457 data we find that:

- Fitting multiple lines *vs.* only fitting one line in some experiments provided marginal improvement *c.f.* A1w1 *vs.* Aw1, A1w2 *vs.* Aw2 but which line was used and the data treatment also influence the magnitude of the bias (*c.f.* the two UNNOFit results).
- MERLIN and ASP-ME default, or A-DEF, results are almost indistinguishable across the metrics, as expected given the heredity of the codes.
- The bias is not just a matter of the quality of the input spectropolarimetric data. Inversions of AR 12457 using *SDO*/HMI input data that account for

ff (SynthIA, VFISV_ABGM, UNNOFit) were by many metrics almost as good as the MERLIN and ASP-ME (default configuration and others) results using *Hinode*/SP input spectral data.

- Optimization method can matter: generally, genetic-algorithm minimization performed slightly better than minimization by least-squares *c.f.* Aw1 *vs.* ALSw1, A-DEF *vs.* ALS, Aw1 *vs.* ALSw1, but this is not a strong result in these tests.
- Weighting differences can influence the results; equal weighting (Aw3) performed the worst (*c.f.* Aw3 *vs.* Aw1, Aw2, and Aw4).
- Explicitly fitting for the fill fraction provides by far the most significant impact to reduce the bias, (*c.f.* ABGM *vs.* PIPE, A-DEF *vs.* ANF, ALS *vs.* ANFLS).

From the analysis of the *SDO*/HMI time-series data (of both plage and spots), we find that:

- The bias clearly manifests in all three local components of the field confirming that bias in B_{\perp} contaminates the determination of the true magnetic vector. When the impact of the B_{\perp} bias is high (*e.g.* PIPE_720s_P11 *vs.* ABGM_720s_P11 results), it is generally high for all metrics across all three B_x^h, B_y^h, B_z^h components.
- The bias can manifest in strong / pixel-filling regions as well as unresolved features. Focusing on *_Sp1 and *_Sp2, while we may expect some evolutionary changes with disk passage, the metrics improve with inversions that fit for ff (*c.f.* ABGM_720S_Sp1 *vs.* PIPE_720S_Sp1).
- Reducing the photon noise (720s *vs.* 5760s) provides a small, but not significant mitigation. Confirming the results of Pevtsov et al. (2021), random photon noise in the data is not the primary source of B_{\perp} bias.
- Explicitly accounting for $ff \neq 1.0$ mitigates the bias, whether through a traditional inversion approach (*c.f.* ABGM_720S_* *vs.* PIPE_720S_*) or by a Neural Net trained on inversion output that itself explicitly accounted for $ff \neq 1.0$ (*c.f.* SYNTHIA_720S_* *vs.* PIPE_720S_*).

4. Post-Facto Quick Fix

Using the assumption that plage is *statistically* dominated by radially-directed field and the fill factor ff is not explicitly set or is otherwise already multiplied-through in the equations below, then we use the most probable image-plane inclination $\mathcal{P}(|\gamma^i|) = \theta$, θ being the observing angle (Svalgaard, Duvall, and Scherrer, 1978; Wang and Sheeley, 1992; Leka, Barnes, and Wagner, 2017), as the basis for evaluation and now, for correction. This “quick-fix” approach is straightforward (see also Rudenko and Dmitrienko, 2018), but should be implemented when concerned with the large-scale averages or contributions across well-measured (sufficient polarization) pixels. The resulting values are not claimed to be “correct” any more than any inversion results are, just less influenced by the bias.

The approach is as follows for under-resolved plage areas:

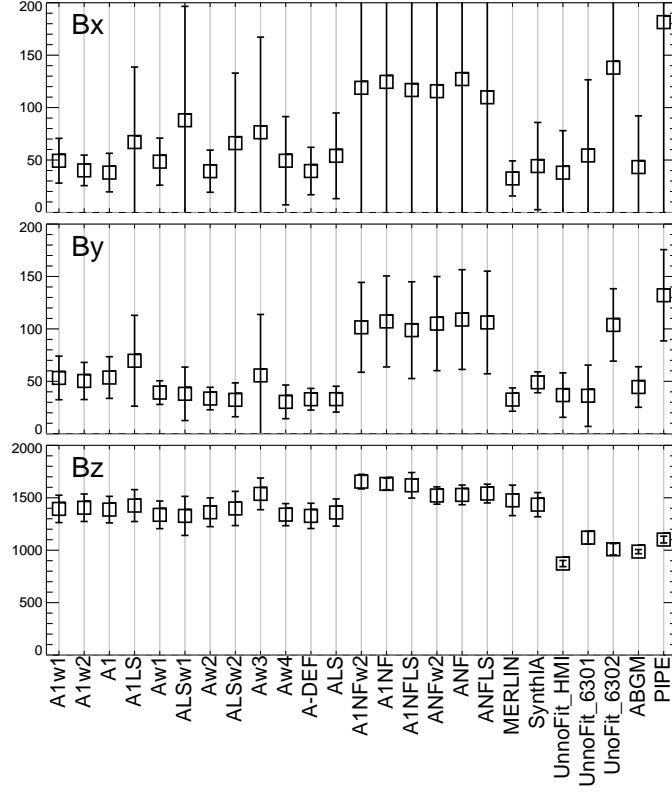


Figure 17. Boxes: the mean absolute separation of the most-probable values over the 6 days; error bars: the standard deviation of the *signed* separation, which will be larger if it changes sign for example. Results (top to bottom) are for B_x^h, B_y^h, B_z^h according to the labels on the x-axis (introduced in Table 2).

- i) Identify plage structures sampled across a range of observing angles $\mu = \cos(\theta)$ (with full-disk data or with a temporal sequence of *statistically* consistent structures).
- ii) Examine the distributions of $|\gamma^i|$ as $f(\mu = \cos(\theta))$ and determine a simple functional form for the systematic angle difference $\Delta|\gamma^i| = \mathcal{P}(|\gamma^i|)(\mu) - \mu$ in appropriate units.
- iii) Assuming that B_{\parallel} should not change, and working initially with the absolute inclination $|\gamma^i|$ and assigning a new inclination $|\gamma^i|' = |\gamma^i| - \Delta|\gamma^i|$, we find

$$B_{\parallel} = |\mathbf{B}| \cos(|\gamma^i|) = |\mathbf{B}'| \cos(|\gamma^i|') \quad (1)$$

$$|\mathbf{B}'| = |\mathbf{B}| \cos(|\gamma^i|') / \cos(|\gamma^i|) \quad (2)$$

$$= \frac{|\mathbf{B}|}{\cos(\Delta|\gamma^i|) + \sin(|\gamma^i|) \sin(\Delta|\gamma^i|) / \cos(\Delta|\gamma^i|)} \quad (3)$$

where the $\Delta\gamma^i$ is the functional form of the deviation of the most probable image-frame inclination from expected as a function of observing angle, and

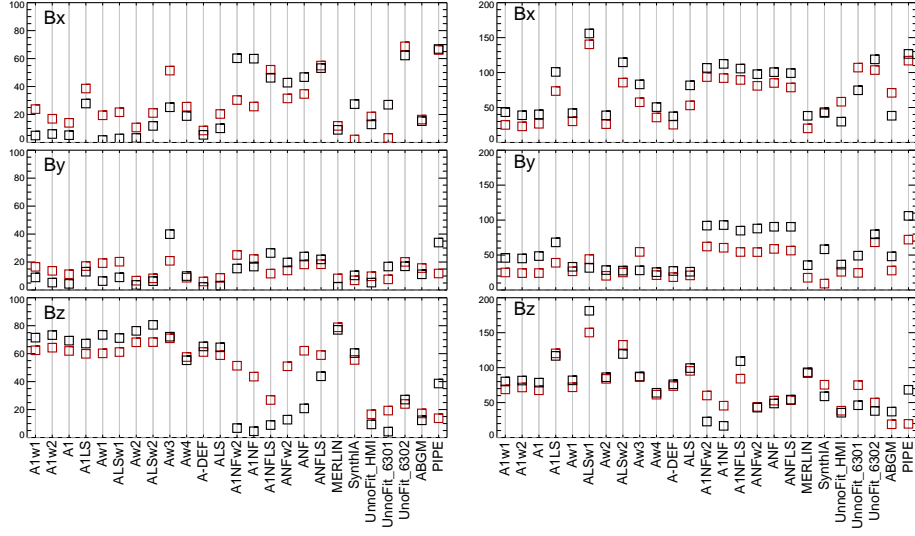


Figure 18. (Left) Median absolute deviation (MAD), and (right) maximum absolute deviation of the most probable values over the 6 samples. Red/Black points are for those with positive / negative underlying B_z^h , respectively.

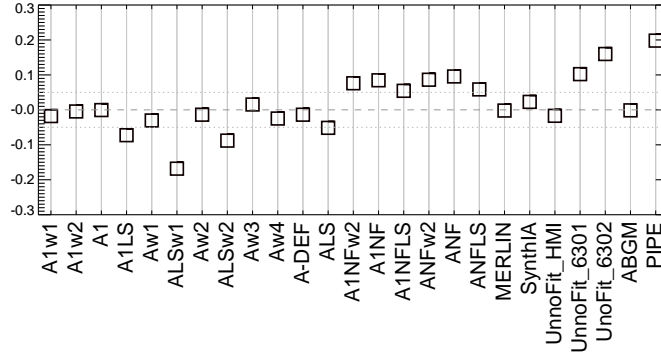


Figure 19. Gini coefficient of the distribution of $|\gamma^i|$ as $f(\mu)$, where the accumulated 6 maps were combined and then points binned according to μ . Gini coefficients within ± 0.05 should show minimal bias.

each pixel is thus “corrected” according to field strength, inclination angle, this function, and the observing location. This formulation can of course be presented in a number of ways, but the important aspects are that (1) if $\Delta|\gamma^i| \rightarrow 0$ that $|\mathbf{B}|$ is recovered, and (2) the results do not become infinite for, *e.g.*, $|\gamma^i| \approx 0$ (if it performs badly near $|\gamma^i| \approx \pi/2$, that will statistically be less of an issue).

Once the total field strength $|\mathbf{B}'|$ is adjusted in this way, we work backwards to find the new inclination angle and the new components:

$$\gamma^{i'} = \cos^{-1}(B_{\parallel}/|\mathbf{B}'|) \quad (4)$$

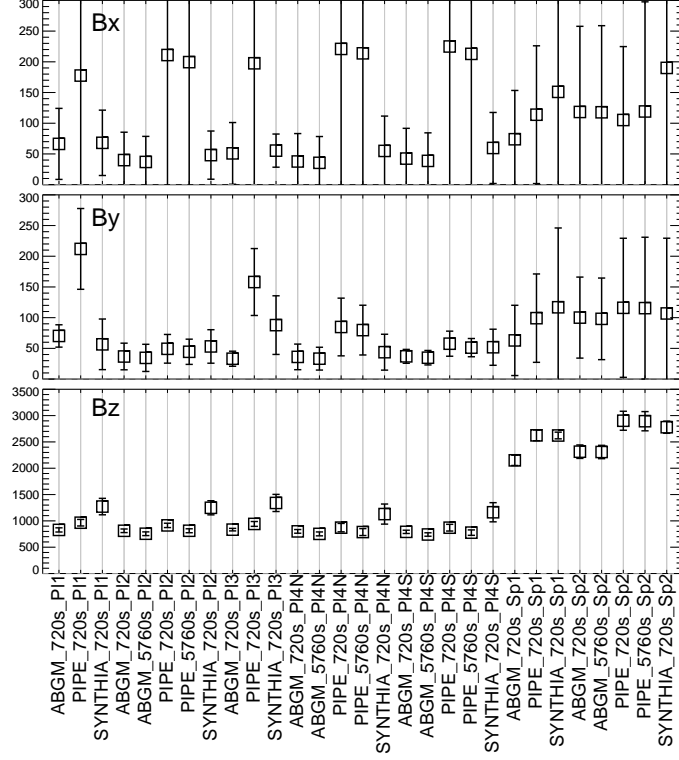


Figure 20. Similar format as Figure 17 for the *SDO*/HMI target patches and inversion options as indicated (labels are introduced in Tables 2, 3, plus the `hmi.S_5760s`-series integration option), computed for their disk transit. Note that the sunspots are unipolar, which will influence the results.

$$B'_{\perp} = |B'| \sin(\gamma^{i'}) \quad (5)$$

where note that in the last two steps, we now use and recover the full $[0, \pi]$ range of γ^i . Again, B_{\parallel} remains the same.

As a demonstration, we find the coefficients of a 2nd-order polynomial fit for $\Delta|\gamma^i|$ to μ from full-disk *SDO*/HMI data for 2010.04, 2010.06 and 2010.08. A 3rd-order fit the sampled regions well, but extrapolated poorly for disk-center corrections. We then apply the above to the Plage 3 time-series extraction (Figures 3, 9). A first try resulted in an over-correction, diagnosed using a most-probable $|\gamma^i|(\mu)$ plot similar to Figure 13, but a simple 25% reduction in the coefficient magnitudes produced a narrow distribution centered well on the $x = y$ line. The disambiguation was then performed and the same diagnostics are used to evaluate this *post-facto* approach. The relevant metrics *c.f.* the results for “PIPE_720s_P13” in Figures 20-22, are listed in the caption for Figure 23 where we show the new time-series plots to compare to Figure 9.

Box plot showing the distribution of the number of iterations for different models and datasets. The y-axis represents the number of iterations, ranging from -0.1 to 0.4. The x-axis lists 24 categories, each representing a model and dataset combination. The categories are: ABGM_720s_P11, PIPE_720s_P11, SYNTHIA_720s_P11, ABGM_720s_P12, ABGM_5760s_P12, PIPE_720s_P12, PIPE_5760s_P12, SYNTHIA_720s_P12, ABGM_720s_P13, PIPE_720s_P13, SYNTHIA_720s_P13, ABGM_720s_P14, ABGM_5760s_P14, PIPE_720s_P14, PIPE_5760s_P14, SYNTHIA_720s_P14, ABGM_720s_P14, ABGM_5760s_P14, PIPE_720s_P14, PIPE_5760s_P14, SYNTHIA_720s_P14, ABGM_720s_Sp1, PIPE_720s_Sp1, SYNTHIA_720s_Sp1, ABGM_720s_Sp2, ABGM_5760s_Sp2, PIPE_720s_Sp2, and PIPE_5760s_Sp2. The plot shows that the number of iterations is generally higher for the P11 and P12 datasets compared to the P13 and P14 datasets, and higher for the ABGM and PIPE models compared to the SYNTHIA model.

5. Concluding Remarks

SOLA: ms_arxiv.tex; 26 July 2022; 3:04; p. 28

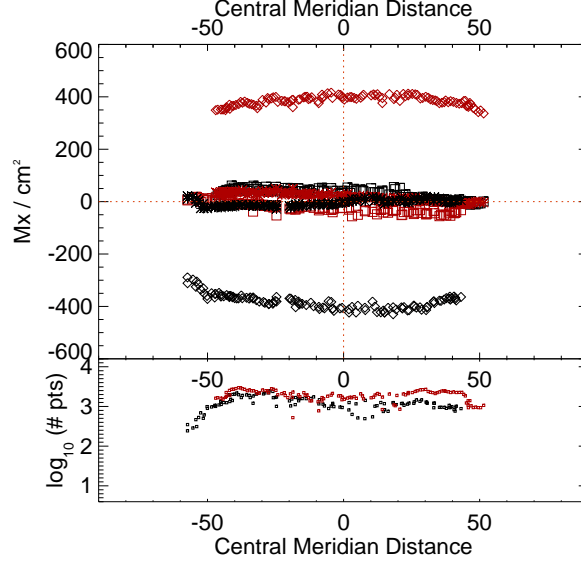


Figure 23. Similar to Figure 9 but after the corrections described in the text. The metrics, for B_x^h , B_y^h and B_z^h respectively are: Mean Absolute Separation: 32.0 ± 25.2 , 57.3 ± 16.6 , 765.6 ± 42.5 ; MAD (for $B_z^h > 0$ / $B_z^h < 0$): 13.5/9.4, 14.7/12.1, 12.7/19.0; MaxAD: 42.4/26.0, 53.2/57.9, 42.5/80.4; Gini: -0.02 , -0.02 .

Previous works on this topic have illustrated that the problem exists, and touched on some compute-intensive approaches to mitigation. In this work we perform four novel investigations and point to potentially less-arduous mitigation approaches.

First, we develop quantitative metrics to measure the B_{\perp} bias. At least one, the Gini-coefficient of the departure from expected image-plane inclination angles in plage features, is applicable without performing the 180° disambiguation, given sufficient sampling of appropriate structures across observing angle. These quantitative metrics are used to point out that the bias in *SDO*/HMI data is not limited to the unresolved plage features; some bias is seen in the strong-field field-filling pixels of sunspots. The quantitative metrics are then available to evaluate and compare data.

Second, we systematically compared the results of different inversion implementation options and targets (different spectral lines used), evaluating the results using common observational targets and the quantitative metrics developed above. We find that the most impactful implementation choice is to include *ff* as an independent parameter in the optimization, or having trained a neural net on such data. Applying inversions that explicitly fit *ff* mitigates bias in plage and in strong-field pixel-filled sunspot centers. That being said, which optimization scheme is used, the weighting used to calculate χ^2 , and the use of multiple spectral lines also impact the outcomes. We also tested a direct comparison of two very different data sources (*Hinode*/SP vs. *SDO*/HMI for NOAA AR 12457) using different inversions both, and found that data source *per se* did not account for the bias.

Third, we construct a simple “toy” model that is appropriate to test certain observed features of the B_{\perp} bias. Experiments were performed which added bias with different functional forms as well as varying the level of photon noise in the data. We show that noise is not the primary contributor to the of the B_{\perp} bias. We could not, however, reconstruct a distinct non-linear aspect visible in the $SDO/HMI |\gamma^i|(\mu)$ behavior. The source and contribution function to the bias is more complex than our experiments. Further refinement to the models to determine the source of this non-linear shape is beyond the scope of this paper.

Fourth and finally, we demonstrate a straightforward “quick fix” that can be applied for analysis of global plage structures on a statistical basis, and can be applied prior to performing the disambiguation step. This *post-facto* algorithm (see also Rudenko and Dmitrienko, 2018), should not take the place of a more robust inversion, and should probably not be used to interpret any individual pixel’s results quantitatively. However, it can be used to produce vector field data for which the bias is adequately removed so as to produce more reasonable global B_{ϕ} , B_{θ} , B_r maps for example.

We show that there are in fact viable options for more robust full-disk inversions of SDO/HMI data: **UNNOFit** (Bommier et al., 2007), the new **VFISV_ABGM** (Grión-Marín et al., 2021) and **SynTHIA** (Higgins et al., 2022). The first two are more traditional implementations of Milne-Eddington codes that explicitly include fill fraction in the optimization, the latter is a neural-net trained on *Hinode*/SP Level-2.0 output and SDO/HMI `hmi.s_720s` [I , Q , U , V] input. Given the vast differential in computing resources required, the latter may be a more readily-available solution, especially for large datasets.

Data Availability Statement

The majority of the data used in this research is sourced from public pipeline-produced products and codes, as cited and referenced; specific time-series cubes, for example, can be made available upon request to the corresponding author. Data from **VFISV_ABGM** are in series `su_abgm.ME.720s_fd10_forKD2` at <http://jsoc2.stanford.edu/ajax/lookdata.html> which requires interested parties to contact the SDO/HMI team for access. Data from **SynTHIA** can be made available upon reasonable request, see also Higgins et al. (2022) and sources therein; KDL, ELW, and RH are actively involved in a project to establish the **SynTHIA** as a publicly-accessible series through JSOC. The **UNNOFit** inversion code is available at <http://lesia.obspm.fr/perso/veronique-bommier>.

Acknowledgments We thank the anonymous referee for very helpful suggestions. KDL and ELW gratefully acknowledge support from NASA GSFC 80NSSC19K0317, NASA/LWS 80NSSC18K0180, from Lockheed-Martin Space Systems contract #4103056734 for Solar-B FPP Phase E, and NASA/HSR 80NSSC18K0065 for developing the custom-extraction codes. We thank Dr. Yang Liu and Dr. Keiji Hayashi for helping identify suitable target regions, Dr. Xudong Sun for running 5760 s SDO/HMI pipeline data, Drs. Ale Pacini and Graham Barnes for helpful discussions, and Dr. David Fouhey for nudging RH, who (with KDL) acknowledges support from the NASA Heliophysics Phase-I DRIVE Science Center (SOLSTICE) at the

University of Michigan under grant NASA 80NSSC20K0600; RH's work was also supported by the Michigan Institute for Data Science via a Propelling Original Data Science grant. ABGM acknowledges support by NASA contract NAS5-02139 (HMI) to Stanford University, and additional support by the Research Council of Norway through its Centres of Excellence Scheme, project No. 262622. VB acknowledges the access granted to the HPC resources of MesoPSL financed by the Region Ile de France and the project Equip@Meso (reference ANR-10-EQPX-29-01) of the programme Investissements d'Avenir supervised by the Agence Nationale pour la Recherche. Some figures in this manuscript were produced using IDL colour-blind-friendly colour tables (see Wright, 2017).

References

- Bommier, V.: 2016, Milne-Eddington inversion for unresolved magnetic structures in the quiet Sun photosphere. *J. Geophys. Res. (Space Phys.)* **121**, 5025. DOI. ADS.
- Bommier, V., Landi Degl'Innocenti, E., Landolfi, M., Molodij, G.: 2007, UNNOFIT Inversion of Spectro-Polarimetric Maps Observed with THEMIS. *Astron. Astrophys.* **464**, 323. DOI. ADS.
- Borrero, J.M., Tomczyk, S., Kubo, M., Socas Navarro, H., Schou, J., Couvidat, S., Bogart, R.: 2010, VFISV: Very Fast Inversion of the Stokes Vector for the Helioseismic and Magnetic Imager. *Solar Phys.*, 35. DOI. ADS.
- Centeno, R., Schou, J., Hayashi, K., Norton, A., Hoeksema, J.T., Liu, Y., Leka, K.D., Barnes, G.: 2014, The Helioseismic and Magnetic Imager (HMI) Vector Magnetic Field Pipeline: Optimization of the Spectral Line Inversion Code. *Solar Phys.* **289**, 3531. DOI. ADS.
- del Toro Iniesta, J.C., Ruiz Cobo, B.: 2016, Inversion of the radiative transfer equation for polarized light. *Living Reviews in Solar Physics* **13**, 4. DOI. ADS.
- del Toro Iniesta, J.C., Orozco Suárez, D., Bellot Rubio, L.R.: 2010, On Spectropolarimetric Measurements with Visible Lines. *Astrophys. J.* **711**, 312. DOI. ADS.
- Griñón-Marín, A.B., Pastor Yabar, A., Liu, Y., Hoeksema, J.T., Norton, A.: 2021, Improvement of the Helioseismic and Magnetic Imager (HMI) Vector Magnetic Field Inversion Code. *Astrophys. J.* **923**, 84. DOI. ADS.
- Henney, C.J., Keller, C.U., Harvey, J.W.: 2006, SOLIS-VSM Solar Vector Magnetograms. In: Casini, R., Lites, B.W. (eds.) *Solar Polarization 4, Astronomical Society of the Pacific Conference Series* **358**, 92. ADS.
- Higgins, R.E.L., Fouhey, D.F., Zhang, D., Antiochos, S.K., Barnes, G., Hoeksema, J.T., Leka, K.D., Liu, Y., Schuck, P.W., Gombosi, T.I.: 2021, Fast and Accurate Emulation of the SDO/HMI Stokes Inversion with Uncertainty Quantification. *Astrophys. J.* **911**, 130. DOI. ADS.
- Higgins, R.E.L., Fouhey, D.F., Antiochos, S.K., Barnes, G., Cheung, M.C.M., Hoeksema, J.T., Leka, K.D., Liu, Y., Schuck, P.W., Gombosi, T.I.: 2022, SynthIA: A Synthetic Inversion Approximation for the Stokes Vector Fusing SDO and Hinode into a Virtual Observatory. *Astrophys. J. Supp. Ser.* **259**, 24. DOI. ADS.
- Hoeksema, J.T., Liu, Y., Hayashi, K., Sun, X., Schou, J., Couvidat, S., Norton, A., Bobra, M., Centeno, R., Leka, K.D., Barnes, G., Turmon, M.: 2014, The Helioseismic and Magnetic Imager (HMI) Vector Magnetic Field Pipeline: Overview and Performance. *Solar Phys.* **289**, 3483. DOI. ADS.
- Ichimoto, K., Lites, B., Elmore, D., Suematsu, Y., Tsuneta, S., Katsukawa, Y., Shimizu, T., Shine, R., Tarbell, T., Title, A., Kiyohara, J., Shinoda, K., Card, G., Lecinski, A., Streander, K., Nakagiri, M., Miyashita, M., Noguchi, M., Hoffmann, C., Cruz, T.: 2008, Polarization Calibration of the Solar Optical Telescope Onboard Hinode. *Solar Phys.* **249**, 233. DOI. ADS.
- Jolliffe, I.T., Stephenson, D.B.: 2012, *Forecast verification: A practitioner's guide in atmospheric science, 2nd edition*, Wiley, The Atrium, Southern Gate, Chichester, West Sussex PO19 8SQ, England. DOI.
- Keller, C.U., The SOLIS Team: 2001, The SOLIS Vector-Spectromagnetograph (VSM). In: Sigwarth, M. (ed.) *Advanced Solar Polarimetry – Theory, Observation, and Instrumentation, Astronomical Society of the Pacific Conference Series* **236**, 16. ADS.

- Kosugi, T., Matsuzaki, K., Sakao, T., Shimizu, T., Sone, Y., Tachikawa, S., Hashimoto, T., Minesugi, K., Ohnishi, A., Yamada, T., Tsuneta, S., Hara, H., Ichimoto, K., Suematsu, Y., Shimojo, M., Watanabe, T., Shimada, S., Davis, J.M., Hill, L.D., Owens, J.K., Title, A.M., Culhane, J.L., Harra, L.K., Doschek, G.A., Golub, L.: 2007, The Hinode (Solar-B) Mission: An Overview. *Solar Phys.* **243**, 3. DOI. ADS.
- LaBonte, B.: 2004, The Imaging Vector Magnetograph at Haleakala : III. Effects of Instrumental Scattered Light on Stokes Spectra. *Solar Phys.* **221**, 191. DOI. ADS.
- Leka, K.D.: 1997, The Vector Magnetic Fields and Thermodynamics of Sunspot Light Bridges: The Case for Field-free Disruptions in Sunspots. *Astrophys. J.* **484**, 900. DOI. ADS.
- Leka, K.D., Barnes, G.: 2012, Modeling and Interpreting the Effects of Spatial Resolution on Solar Magnetic Field Maps. *Solar Phys.* **277**, 89. DOI. ADS.
- Leka, K.D., Barnes, G., Crouch, A.: 2009, An Automated Ambiguity-Resolution Code for Hinode/SP Vector Magnetic Field Data. In: B. Lites, M. Cheung, T. Magara, J. Mariska, & K. Reeves (ed.) *The Second Hinode Science Meeting: Beyond Discovery-Toward Understanding*, *Astronomical Society of the Pacific Conference Series* **415**, 365. ADS.
- Leka, K.D., Barnes, G., Wagner, E.L.: 2017, Evaluating (and Improving) Estimates of the Solar Radial Magnetic Field Component from Line-of-Sight Magnetograms. *Solar Phys.* **292**, 36. DOI. ADS.
- Leka, K.D., Barnes, G., Wagner, E.L.: 2018, The NWRA Classification Infrastructure: Description and Extension to the Discriminant Analysis Flare Forecasting System (DAFFS). *Journal of Space Weather and Space Climate* **8**, A25. DOI.
- Lites, B.W., Skumanich, A.: 1990, Stokes Profile Analysis and Vector Magnetic Fields. V - The Magnetic Field Structure of Large Sunspots Observed with Stokes II. *Astrophys. J.* **348**, 747. DOI. ADS.
- Lites, B.W., Leka, K.D., Skumanich, A., Martinez Pillet, V., Shimizu, T.: 1996, Small-Scale Horizontal Magnetic Fields in the Solar Photosphere. *Astrophys. J.* **460**, 1019. DOI. ADS.
- Lites, B.W., Akin, D.L., Card, G., Cruz, T., Duncan, D.W., Edwards, C.G., Elmore, D.F., Hoffmann, C., Katsukawa, Y., Katz, N., Kubo, M., Ichimoto, K., Shimizu, T., Shine, R.A., Streander, K.V., Suematsu, A., Tarbell, T.D., Title, A.M., Tsuneta, S.: 2013, The Hinode Spectro-Polarimeter. *Solar Phys.* **283**, 579. DOI. ADS.
- Liu, Y., Griñón-Marín, A.B., Hoeksema, J.T., Norton, A.A., Sun, X.: 2022, On the Hemispheric Bias Seen in Vector Magnetic Field Data. *Solar Phys.* **297**, 17. DOI. ADS.
- Metcalf, T.R.: 1994, Resolving the 180-degree Ambiguity in Vector Magnetic Field Measurements: The 'Minimum' Energy Solution. *Solar Phys.* **155**, 235. DOI.
- Orozco Suárez, D., Katsukawa, Y.: 2012, On the Distribution of Quiet-Sun Magnetic Fields at Different Heliocentric Angles. *Astrophys. J.* **746**, 182. DOI. ADS.
- Pesnelli, W.D., Thompson, B.J., Chamberlin, P.C.: 2012, The Solar Dynamics Observatory (SDO). *Solar Phys.* **275**, 3. DOI. ADS.
- Pevtsov, A.A., Liu, Y., Virtanen, I., Bertello, L., Mursula, K., Leka, K.D., Hughes, A.L.H.: 2021, On a limitation of Zeeman polarimetry and imperfect instrumentation in representing solar magnetic fields with weaker polarization signal. *Journal of Space Weather and Space Climate* **11**, 14. DOI. ADS.
- Press, W.H., Teukolsky, S.A., Vetterling, W.T., Flannery, B.P.: 1992, *Numerical recipes: The art of scientific computing*, 2nd edn. Cambridge University Press, New York.
- Ronan, R.S., Mickey, D.L., Orrall, F.Q.: 1987, The Derivation of Vector Magnetic Fields from Stokes Profiles: Integral vs. Least Squares Fitting Techniques. *Solar Phys.* **113**, 353.
- Rudenko, G., Dmitrienko, I.: 2018, The presence of a systematic error in SDO/HMI data. *Solar-Terr. Phys.* **4**, 3. DOI. ADS.
- Sainz Dalda, A.: 2017, A Statistical Comparison between Photospheric Vector Magnetograms Obtained by SDO/HMI and Hinode/SP. *Astrophys. J.* **851**, 111. DOI. ADS.
- Sanchez Almeida, J.: 1997, Physical Properties of the Solar Magnetic Photosphere under the MISMA Hypothesis. I. Description of the Inversion Procedure. *Astrophys. J.* **491**, 993. DOI. ADS.
- Scherrer, P.H., Schou, J., Bush, R.I., Kosovichev, A.G., Bogart, R.S., Hoeksema, J.T., Liu, Y., Duvall, T.L., Zhao, J., Title, A.M., Schrijver, C.J., Tarbell, T.D., Tomczyk, S.: 2012, The Helioseismic and Magnetic Imager (HMI) Investigation for the Solar Dynamics Observatory (SDO). *Solar Phys.* **275**, 207. DOI. ADS.
- Schou, J., Scherrer, P.H., Bush, R.I., Wachter, R., Couvidat, S., Rabello-Soares, M.C., Bogart, R.S., Hoeksema, J.T., Liu, Y., Duvall, T.L., Akin, D.J., Allard, B.A., Miles, J.W., Rairden, R., Shine, R.A., Tarbell, T.D., Title, A.M., Wolfson, C.J., Elmore, D.F., Norton, A.A., Tomczyk, S.: 2012, Design and Ground Calibration of the Helioseismic and Magnetic Imager

- (HMI) Instrument on the Solar Dynamics Observatory (SDO). *Solar Phys.* **275**, 229. DOI. ADS.
- Schuck, P.W., Antiochos, S.K., Leka, K.D., Barnes, G.: 2016, Achieving Consistent Doppler Measurements from SDO/HMI Vector Field Inversions. *Astrophys. J.* **823**, 101. DOI. ADS.
- Skumanich, A., Lites, B.W.: 1987, Stokes Profile Analysis and Vector Magnetic Fields. I - Inversion of Photospheric Lines. *Astrophys. J.* **322**, 473. DOI. ADS.
- Socas Navarro, H.: 2004, Multiline Stokes Analysis for the Study of Small-Scale Solar Magnetic Fields. *Astrophys. J.* **613**, 610. DOI. ADS.
- Sun, X., Liu, Y., Milić, I., Griñón-Marín, A.B.: 2021, Are the Magnetic Fields Radial in the Solar Polar Region? *Res. Notes Am. Astron. Soc.* **5**, 134. DOI. ADS.
- Svalgaard, L., Duvall, T.L. Jr., Scherrer, P.H.: 1978, The Strength of the Sun's Polar Fields. *Solar Phys.* **58**, 225. DOI. ADS.
- Tsuneta, S., Ichimoto, K., Katsukawa, Y., Nagata, S., Otsubo, M., Shimizu, T., Suematsu, Y., Nakagiri, M., Noguchi, M., Tarbell, T., Title, A., Shine, R., Rosenberg, W., Hoffmann, C., Jurcevich, B., Kushner, G., Levay, M., Lites, B., Elmore, D., Matsushita, T., Kawaguchi, N., Saito, H., Mikami, I., Hill, L.D., Owens, J.K.: 2008, The Solar Optical Telescope for the Hinode Mission: An Overview. *Solar Phys.* **249**, 167. DOI. ADS.
- Wang, Y., Sheeley, N.R. Jr.: 1992, On Potential Field Models of the Solar Corona. *Astrophys. J.* **392**, 310. DOI. ADS.
- Westendorp Plaza, C., del Toro Iniesta, J.C., Ruiz Cobo, B., Martinez Pillet, V., Lites, B.W., Skumanich, A.: 1998, Optical Tomography of a Sunspot. I. Comparison Between Two Inversion Techniques. *Astrophys. J.* **494**, 453.
- Wright, P.: 2017, *ColourBlind: A Collection of Colour-blind-friendly Colour Tables*, Zenodo. DOI. ADS.